fiber only (Bannon 2009) and on hybrid glass and carbon composites (Demkowicz 2011), predicting modulus to within 10%.

An important parameter in CLT is the fiber volume fraction, V_f, the percentage of a given volume of laminate that is fibers (for a vacuum infusion process it is assumed that the remaining volume is resin). Prior research on the arches has assumed a 50% fiber volume fraction (Bannon, 2009). There are techniques to directly measure fiber volume fraction such as acid digestion, and while it would be valuable to experimentally obtain this value, it is beyond the scope of present research. Also, this thesis deals entirely with arch or tube sections, not representative plate sections (comprised of the same laminates as an arch, but left as a flat plate), and in arch sections there is a large amount of surplus resin from flow media and infusion lines that contributes weight to a specimen but does not contribute to the layer thickness. The extra resin contributes little to the longitudinal or radial modulus, but it adds resin mass and changes the measured fiber volume fraction. As detailed later in this chapter, specimen thickness was measured carefully to avoid any resin ridges or other resin-rich portions of the tube. This presented another technique to find V_f. For a group of 6.50in tubes the length L_l and weight W_l of both the carbon fiber and the glass fiber was measured during fabrication; with a post infusion thickness t and diameter $2r$ the total volume V_l of a carbon fiber or glass fiber layer was calculated in Equation 3

.

$$V_l = 2r\pi L_l t_l \qquad \text{Equation 3}$$

With known densities ρ for both materials, it was possible to find the weight of a layer, if entirely fiber, and with that weight and the measured fiber weight calculate the fiber volume fraction in Equation 4

.

$$V_f = \frac{W_l}{V_l \rho} \qquad \text{Equation 4}$$

All of the input values for this analysis are in Table 13. This analysis shows that for mass of fiber to be conserved, for the measured thickness and diameter, fiber volume fraction for both the carbon and the glass should be 56%, which is 12% higher than the previous assumed value. Both layers independently indicated the same fiber volume fraction, lending confidence in its accuracy. Fiber volume fraction has been measured to be between 49% and 53% in plates made from woven E-glass reinforced sheets using the

This test report shall not be reproduced, except in full, without the written approval of
the AEWC Advanced Structures & Composites Center.

same vinyl ester resin and the same vacuum infusion process (El-Chiti, 2005). The differences between the process used by El-Chiti and the arch fabrication process could account for the difference in fiber volume fraction. Another difference is thickness measurement technique; a caliper has a long jaw that spans the top of several fiber tow bundles. All measurements in tubes were taken with a fine ball micrometer to avoid resin ridges and flow media that create an artificial thickness. The ball micrometer was placed at thin points between fiber tows instead of measuring across the top, reducing the measured thickness and increasing V_f.

Table 13 Properties for Determining Fiber Volume Fraction

Material	**2*r* (in)**	**L_l (ft)**	**t_l (in)**	**W_l (lb)**	**ρ (lb/in^3)**	**V_f (%)**
Carbon	6.50	41.3	.027	10.0	.065	56.0
Glass	6.46	37.4	.035	16.5	.092	56.4

The areal weight of the fabric at the use angle is provided by the manufacturer; this value depends on the density and the thickness of the material. As seen in Table 14, the predicted weight was very close to the experimental for the carbon, but was different for the glass fiber braid. This value was used for calculating fiber volume fraction when individual material weights were not available (Demkowicz, 2011).

Table 14 Predicted and Measured Areal Weight

Areal Weight (PSF)	**Glass**	**Carbon**
Predicted	.391	.143
Measured	.261	.142

Another assumption used in all CLT models was that each braided layer counted as two opposing angle orthotropic plies that each occupies the full depth of the laminate and contributes 50% of the laminate properties. For a braided carbon fiber with 22-degree fiber angle and infused thickness of 0.027in, the total composite was treated as the arithmetic mean of a +22-degree 0.027in layer and a –22-degree 0.027in layer. Typically, a braided composite is treated as two opposing angle plies that each occupy half of a layer; for calculating the extensional compliance matrix both this method and the previous method produce the same result, but when a combined bending and extensional matrix is included the latter method introduces a false torsion-extension term. For calculating the longitudinal and radial moduli, the bending compliance matrix and the combined compliance matrix were ignored (Demkowitz, 2011).

This test report shall not be reproduced, except in full, without the written approval of
the AEWC Advanced Structures & Composites Center.

Preparing Specimens

Large tubes were cut into short sections for axial compression testing using a horizontal band saw to produce planar perpendicular faces. Due to the slight curvature of the beams and the resin ridges on the surface, the cuts were planar but not necessarily parallel to each other or perpendicular to the longitudinal axis of the tube. The 6.50in diameter tubes were cut to 15.0in length while 11.8in and 14.76in tubes were cut to 18.1in and 29.9in lengths, respectively. Figure 39 shows all three different size specimens tested.

Figure 39 - Comparison of Different Size Specimens

Specimen height was measured at four evenly spaced points along the tube circumference. To determine that the points were evenly spaced the centerline circumference was measured using a cloth tape. The thickness of each specimen was measured at eight locations, four on each end of the tube. Thickness was measured using a 0.126in diameter ball micrometer. The thickness measurement was taken at the thinnest section within a diamond of the flow media as an attempt to capture the fiber thickness, staying away from resin ridges and the resin thickened areas near the flow media.

Table 15 contains the average thickness of each full 6.50in tube based on the eight measurements per specimen. Table 16 contains the same information pertaining to 14.4in diameter specimens. The coefficient of variability (COV) of specimen averages indicates the variability between the average thicknesses of each individual specimen. The COV of all measurements indicates the variability of all measurements taken on a single long tube.

This test report shall not be reproduced, except in full, without the written approval of
the AEWC Advanced Structures & Composites Center.

Table 15 Thickness of 6.50in Diameter Tubes

Tube	Number of Measurements	Thickness (in)	COV (%) of Specimen Averages	COV (%) of All Measurements
SC 165, 1	128	.063	3.6	7.5
SC 165, 2	96	.062	3.5	11
SC 165, 3	40	.063	2.0	7.8
SC 165, 4	32	.059	1.2	6.2
BC 165	80	.092	4.1	6.6
DC 165	80	.089	1.3	4.9

Table 16 Thickness of 14.4in Diameter Tubes

Tube	Number of Measurements	Thickness (in)	COV (%) of Specimen Averages	COV (%) of all Measurements
BC 365	32	.122	4.3	7.2
BC 365-76	32	.122	5.6	7.5

The COV of specimen averages is lower for all tubes than the COV of all measurements indicating that the average thickness for all specimens was more consistent than the measurements taken within a single specimen. Longitudinal position in the tube and distance from infusion port has less effect on the thickness than cross section variability. Local thickness variability can be caused by thinner fibers or thinner resin coat and is a potential source of stress concentrations.

Instrumentation

Several setups for the instrumentation were used before deciding on the final version used for the remainder of the specimens. For 11.8in specimens, two +/-0.512in LVDTs (linear voltage differential transducers) were mounted to wooden holders attached to opposing faces of the cylinder with cyanoacrylate. Using two measurement devices produced unreliable data because it was difficult to see how the displacement varied around the entire perimeter of the specimen. For 6.50in and 14.76in diameters, four 1.0in potentiometers measured deflection. Figure 40 through Figure 42 show typical instrumented specimens.

This test report shall not be reproduced, except in full, without the written approval of
the AEWC Advanced Structures & Composites Center.

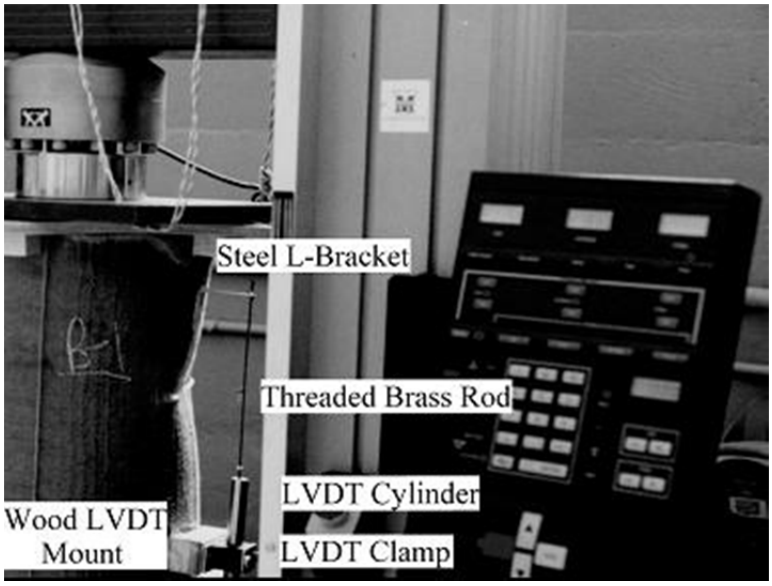

Figure 40 - Instrumentation of an 11.8in specimen

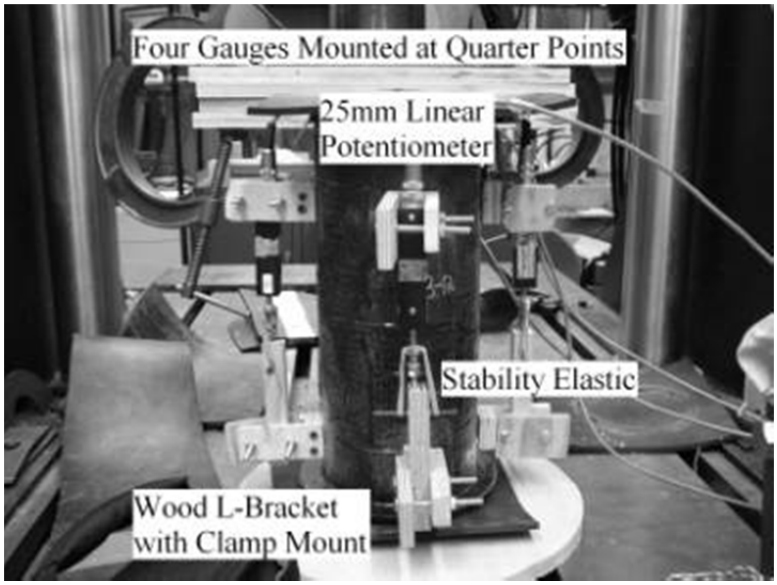

Figure 41 - Instrumentation of a 6.50in Specimen

This test report shall not be reproduced, except in full, without the written approval of the AEWC Advanced Structures & Composites Center.

Figure 42 - Instrumentation on 14.76in Specimen

To attach the potentiometers, L-brackets were constructed from wood with a height of 3.54in and a bottom leg of 0.984in plus the 0.295in to 0.492in thickness of the top leg. These two sections were connected with screws such that the long leg overhung the short leg by approximately 0.098 – allowing two gluing points on a round tube. Two L-brackets were attached 10.8in apart (outside edge to outside edge) for 6.50in tubes and 24.0in apart for 14.76in diameter tubes at quarter points on the perimeter of the cylinder. The bottom bracket held a wooden bearing rod and the top bracket held a 1.0 potentiometer. Both were clamped in place by a wooden plate and two 1/4x20 bolts. The potentiometers used required approximately a 0.9lbs force to either extend or retract. To overcome the initial force the gauge was held in contact to the wooden bearing surface with a rubber elastic. The elastic gave an initial compressive force that reduced a preload period where the gauge did not move despite the specimen moving. The elastics had an additional benefit of giving out of plane rigidity to the gauge. The centerline of the gauges were mounted approximately 1.57in from the side of the tube, meaning that for direct compression the gauges read the appropriate strain but when the specimen experienced bending they moved more than the cross section and were influenced by pinching and opening angles. As a result, the gauge with the largest deflection typically has a bent inward response and the gauge with the least compression (in some cases tension) has a bent outward response.

This test report shall not be reproduced, except in full, without the written approval of
the AEWC Advanced Structures & Composites Center.

The failure time for a specimen was targeted at 2 minutes to 20 minutes to be within the static testing range. Tests were conducted in deflection control. The rate of actuator descent was set depending on the specimens and the boundary conditions. Different boundary conditions are compared in Walton (2011). For stiffer boundaries (steel, FRP) the load rate needed to be lower than for deformable boundaries (plywood, neoprene). For the 11.8in specimens, loads were recorded by a 45kip load cell on a 45kip capacity screw-drive actuator that moved at 0.1in/minute. For 6.50in and 14.76in specimens, loads were recorded with a 110kip load cell mounted on a 110kip capacity hydraulic actuator. Load rate for the 14.76in specimens was 0.2in/minute. 6.50in specimens had a variety of load rates depending on the boundary conditions. In general, plywood specimens were loaded at 0.10in/minute while resin capped specimens were loaded at 0.025in/minute, but this value was changed depending on other layers used in the boundary for load distribution such as neoprene or plywood.

Results, Analysis, and Observations

The primary goal of testing was to get ultimate strength values to be used as a comparison to model predictions, bend test results, and inputs for future modeling. A secondary goal of testing was to find a preferred test configuration to be used on future testing to minimize the uneven loading observed through differential deflection measurements, failure mode, and failure load. Terms used to describe the observed failure are defined, the variation in boundary conditions is explained, the failure strength results is presented, the instrument deflection results are presented, the elastic modulus calculation is explained and the effect of certain defects on ultimate strength – holes and diameter fluctuation glass fibers – are discussed.

Terminology

The location of the failure and the speed of failure were chosen to characterize the failure mode of the FRP cylinders. Both are indications of the uniformity of boundary conditions (loading). The three locations of failure were:

> Bearing failure: Specimen failed at the boundary-characterized by delamination of the glass and carbon layers at the edge of the specimen. The specimen did not buckle. See Figure 43.

This test report shall not be reproduced, except in full, without the written approval of the AEWC Advanced Structures & Composites Center.

Figure 43 - Tube After Bearing Failure

Bearing-buckling failure: Specimen failed either below the bottom gauge or above the top gauge. This failure may have incorporated a certain amount of bearing damage after initial failure, but shows clear evidence of buckling and initial failure is approximately 0.591in to 1.97in from the specimen edge. See Figure 44.

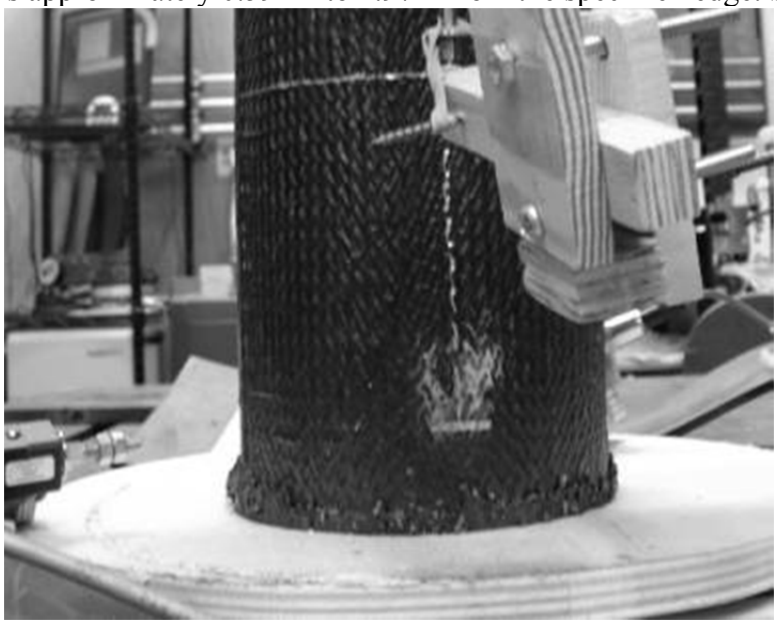

Figure 44 - Bearing-Buckling Failure

This test report shall not be reproduced, except in full, without the written approval of
the AEWC Advanced Structures & Composites Center.

Buckling failure: Specimen failed far enough away from a boundary that no evidence of the failure existed at the boundary or at the plate level. See Figure 45.

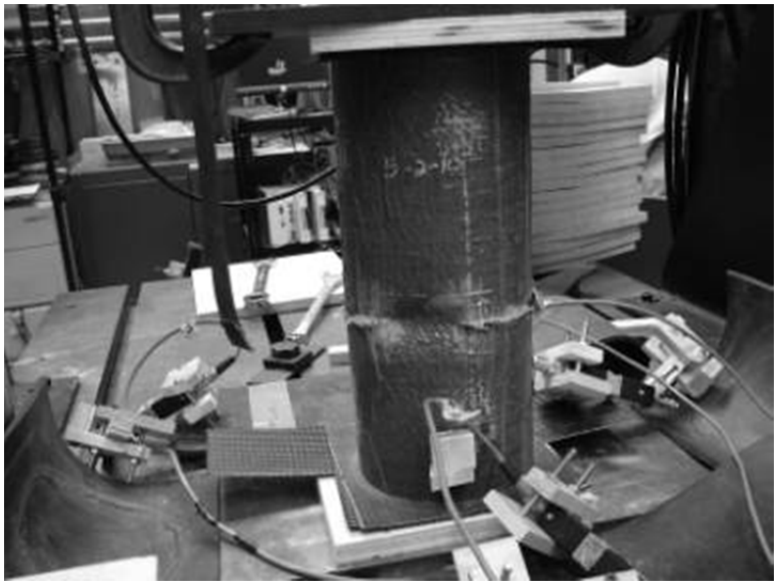

Figure 45 - Buckling Failure

The three failure rate definitions are:

Progressive slow: Specimen buckled in a single location, continued to carry additional load, and more than five seconds passed before the specimen buckled further. This failure rate showed uneven loading where other areas of the specimen were able to hold the capacity of the failed section for a prolonged time. In many cases the ultimate load was reached after the first buckle. See Figure 46 for a typical load-deflection plot.

This test report shall not be reproduced, except in full, without the written approval of the AEWC Advanced Structures & Composites Center.

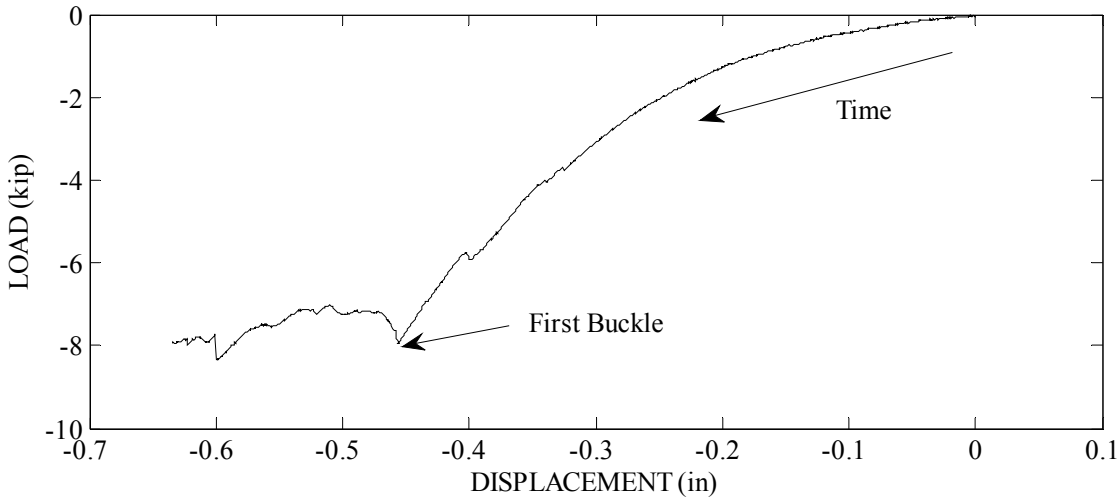

Figure 46 - Load-Displacement for Progressive-Slow Specimen SC 165, 1-13

Progressive rapid: Specimen buckled in a single location and within the next five seconds buckled around perimeter greatly reducing carrying capacity. This failure rate generally coincided with relatively uniform loading as measured by the LVDTs. It was possible that in a load controlled or gravity controlled test, specimens that failed at a progressive rapid rate would fail suddenly because they rarely were able to hold a higher load than initial buckling load. See Figure 47 for a typical load-deflection plot.

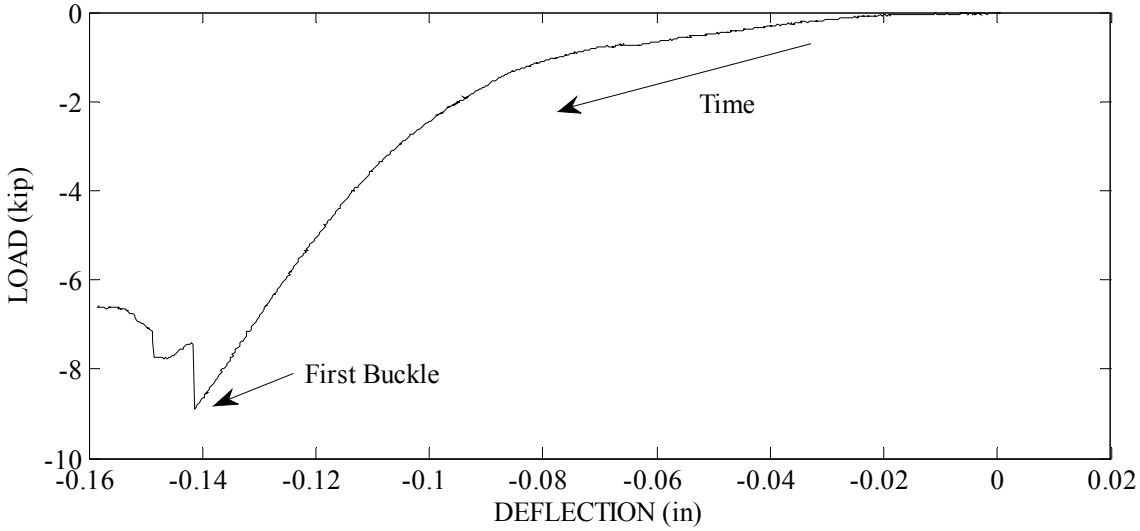

Figure 47 - Load-Displacement for Progressive-Rapid Specimen SC 165, 1-2

This test report shall not be reproduced, except in full, without the written approval of
the AEWC Advanced Structures & Composites Center.

Sudden: Specimen lost carrying capacity and buckled in multiple locations within an indistinguishable time. This failure rate showed very close to uniform loading. See Figure 48 for a typical load-deflection plot.

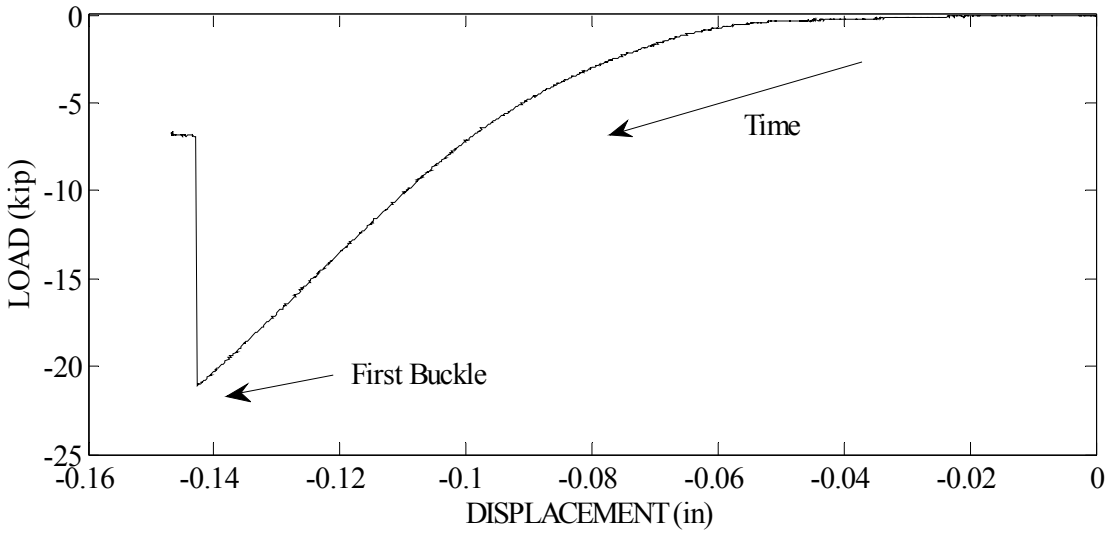

Figure 48 - Load-Displacement for Sudden Buckling Specimen SC 165, 1-6

Boundaries

Boundary conditions were modified and improved during the test series to produce the most reliable and repeatable test. Tests were evaluated on ease of implementation, percentage of sudden failures (a measure of even loading), and uniformity of strain. Two end restraint conditions were tested: fixed-fixed (with two perpendicular plates) or fixed-pin with a top plate that was fixed and a bottom plate mounted on a swiveling ball that was free to rotate as seen in Figure 49. Testing indicated that the specimens with the ball failed early as a result of having a large bending component. The bending component was due to out of plane loading caused by locally softer response in different sides of the specimen or bending and movement of the specimen in the direction normal to the shell.

This test report shall not be reproduced, except in full, without the written approval of the AEWC Advanced Structures & Composites Center.

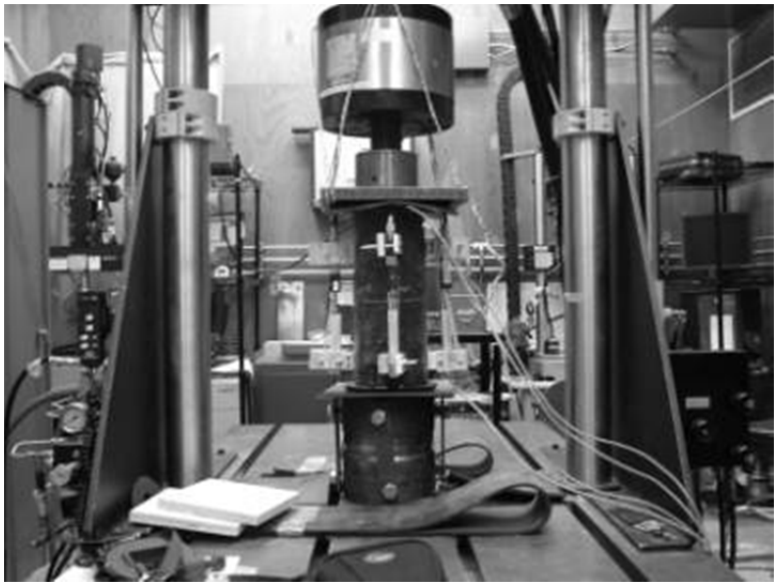

Figure 49 - Specimen Tested with Pivoting Bottom Surface

Four bearing surfaces were used: steel, resin, plywood, and FRP; as well as three materials for under layers between the cross head or table and the specimen: steel, wood, and neoprene. The best boundary condition was obtained with plywood, which crushed before tube rupture and allowed loads to distribute. Performance improved when an infused carbon fiber sheet was placed between the specimen and the plywood delaying the crushing failure and activating a larger crush area. This prevented excessive crushing in high buckling capacity specimens. Details on the different boundary conditions used are in Walton (2011).

Failure Strength

In compression it was possible for a specimen to fail in a localized segment while other segments continued to hold the same or higher compressive load. Bending failures cannot reload; the change in section modulus from cross sectional buckling makes any bending failure irrecoverable. For compression, the failure strength was categorized as the load at which the first buckling or bearing failure occurred. Table 17 contains the average failure load and the coefficient of variation for each type of specimen tested as well as the average of all single layer specimens. Also listed is the number of specimens tested as well as the number of specimens included in the average. For the results of every specimen tested as well as the load deflection plot and instrument deflection plot see Walton (2011).

This test report shall not be reproduced, except in full, without the written approval of
the AEWC Advanced Structures & Composites Center.

Specimens were rejected from Table 17 for three reasons: a ball support was used, the resin cap cracked prior to failure, or the specimen failed in bearing. Testing with a pivoting load or ball support caused highly variable stresses that were read by the gauges as in-plane bending. This was visible in a graph such as Figure 50 below that shows a gauge reading tension in an axial compression test. The progressive slow failure rate for all specimens with this support type is further evidence that the specimens were not experiencing a symmetric load. The ball introduced out of plane bending stresses from a non-axial load that were small but significant due to the relative weakness of the specimen in that loading direction. Use of this fixture also resulted in a significant reduction in failure load.

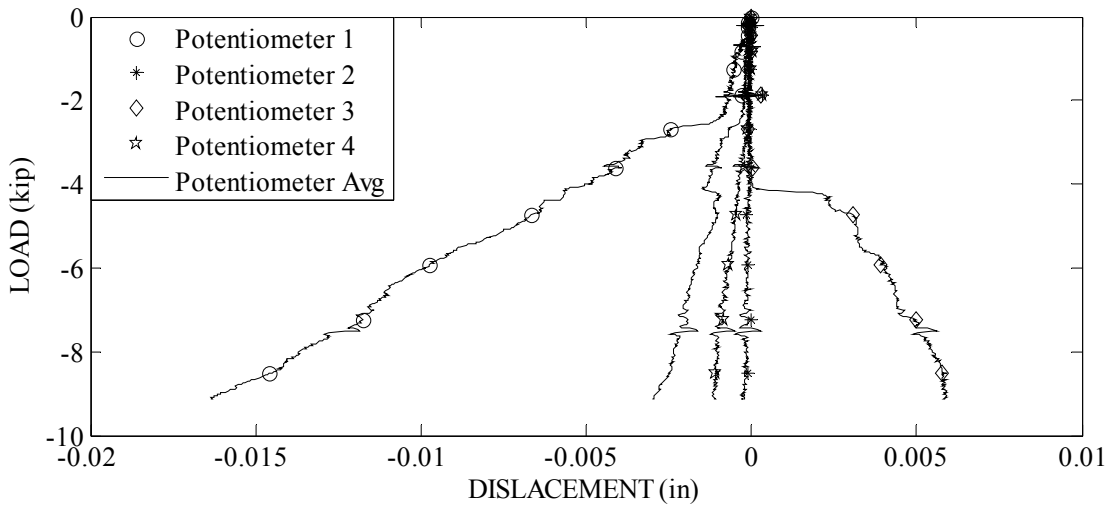

Figure 50 - Specimen SC 165, 1-8 Instrument Displacement Versus Load

Any specimen tested with a resin cap where the cap cracked prior to failure was likely to have sustained end damage on the interface with the resin. This made some specimens fail in bearing instead of buckling. Also, those specimens that did not fail in bearing were likely to fail at a lower load from having an uneven end condition from partially broken resin. Uneven loading of broken resin caps introduced many progressive-slow failures that were a symptom of highly irregular loading.

Specimens were also removed if they failed in bearing, a failure mode with different characteristics that was dependent on local discontinuities and hardness. Bearing failure was a delamination or crushing of the specimen edge and specimens tested with direct contact to steel plates failed in this mode because the material did not accommodate the tube. Other boundaries yielded at the specimen edge. Once the specimen started to crush it would delaminate to reduce load rather than buckle. Issues such as lack of smoothness

This test report shall not be reproduced, except in full, without the written approval of
the AEWC Advanced Structures & Composites Center.

of the specimen edge caused local stress concentrations on the edge of the cylinder that resulted in bearing failure. Bearing failure could be a sudden failure and in some circumstances occurred at a load similar to the buckling load, however it was not the failure mode that was tested for and it therefore was not included in the calculation of the average and COV of the local buckling strength.

The ultimate load did include specimens that failed in either buckling or combined bearing/buckling as they were both local buckling failures and there was not a significant difference in the relative strength of the two failure modes.

Table 17 Failure Strength of 6.50in specimens

6.50in Specimens	Load (Kip)	COV	Number Tested	Number Included
SC 165, Tube 1	16.1	13.2	16	7
SC 165, Tube 2	13.5	19.0	12	8
SC 165, Tube 3	18.7	10.8	5	4
SC 165, Tube 4	14.7	14.1	4	3
SC 165, All Tubes	15.5	18.5	37	22
BC 165	23.2	13.4	14	12
DC 165	30.8	5.07	10	8

The specimens built with double carbon fiber have slightly higher than double the strength of single carbon layer specimens. This was not because the carbon was the only component contributing strength. An added polyester bleeder layer provided a ~50% increase in strength over single carbon by including a layer that had much less stiffness than either the carbon or the off axis e-glass. The results for the bleeder specimens show that increasing wall thickness without making much change to the relative modulus (elastic modulus independent of thickness) increased strength. The bleeder layer and the outer carbon layer both provide an increase in shape stability that increased the buckling load and they bridged gaps or imperfections in the inner layer of carbon, giving better coverage than a single layer of carbon. The second carbon layer provides an additional increase in strength by providing an increase in modulus as seen in later sections. The double carbon specimens had a low COV and a consistent failure mode; seven of eight failed in bearing-buckling.

Global buckling for a column is Euler buckling (Gere, 2004). For a column with pin-pin end conditions, the critical buckling load P_{cr}, Equation 5

This test report shall not be reproduced, except in full, without the written approval of the AEWC Advanced Structures & Composites Center.

, requires the longitudinal elastic modulus E_x, the moment of inertia I and the length of the column L.

$$P_{cr} = \frac{\pi^2 E_x I}{L^2} \qquad \text{Equation 5}$$

For the single-carbon, short-column compression tests, the resulting critical buckling load was 1170kip; two orders of magnitude above the actual buckling load. Because of the large difference in actual buckling and global buckling, it is unlikely that failure occurred in the combined local-global region indicating that the specimen failed in pure local buckling, as intended.

Instrument Deflection

For 11.8in diameter specimens two LVDTs were used to measure deflection. From these two gauges it was impossible to determine the shape of the load distribution but it was thought to be planar due to the two planar faces of the cylinder. To address this uncertainty, testing on the other two diameter specimens was performed with four deflection gauges to observe stress distribution through variation in deflection. If stresses were planar, the most deflected gauge would be opposed by the least deflected gauge and the average deflection of opposing gauges 1 and 3 would be close to the average of 2 and 4. Of the 64 specimens tested only 23 had the highest deflection gauge opposing the lowest deflection gauge at 90% of peak load. Only 18 of the 43 specimens with good load-deflection data had opposing slopes within 25% of each other. Based on this it can be concluded that the majority of specimens did not load with a planar load or did not respond with even axial stiffness around the entire perimeter.

Calculating Elastic Modulus

The FRP shell was assumed linear elastic, meaning that the strain and the stress were related by a constant elastic modulus. FRP is typically assumed to be a linear elastic material because the fibers are linear elastic. The polymer matrix is not linear elastic, but the fibers have a much higher contribution of stiffness to the laminate. The fiber response is more characteristic of the total response. Elastic modulus is presented in terms of stress times length (ksi-in) or relative modulus, ignoring the thickness of the specimens. This is because thickness was highly variable within the same specimen. As mentioned, in the Instrument Deflection section, the measured deflection of the individual gauges was not linear because the loads were irregular and there was a bending response. The bending response tended to cause one gauge to pinch inward (compress) while its opposite gauge extended outward (tense) making the average of two gauges

This test report shall not be reproduced, except in full, without the written approval of
the AEWC Advanced Structures & Composites Center.

include only the axial deflections, not the bending deflections. Averaging the four evenly spaced gauges gave the best attainable deflection.

Several of the first specimens tested were instrumented with a faulty gauge configuration and either the gauge broke away from the specimen prior to failure or lacked the rigidity to remain vertical, so only 43 of the 57 6.50in specimens tested were considered for calculating elastic modulus. The gauges exhibited a relatively high load to deformation compared to other instrumentation, (about 0.9lbs to get the gauge to move,) so a certain amount of deflection needed to occur before any gauges moved. Because the initial load was biased, based on the slight height irregularities of many specimens, the early loading period with a false stiff response lasted until 30% or less of ultimate load. Prior to failure, out of plane motions became large as specimens started to buckle; to avoid this effect no data beyond 90% of ultimate load was used for calculating elastic modulus. Elastic modulus was calculated as the slope of the average deflection-load plot from 30% to 90% of ultimate load multiplied by the gauge length (a constant for all specimens of the same type) and divided by the cross sectional perimeter. Figure 51 is a typical plot of load vs. instrument deflection, for specimen BC 165, 1-9, one of the 6.50in diameter bleeder-carbon tubes with a gauge length of 9.45in. Constant load bars were added at 30% and 90% of maximum load, the duration used for calculating elastic modulus. This plot shows the initially stiff response and illustrates the method of computing the elastic modulus.

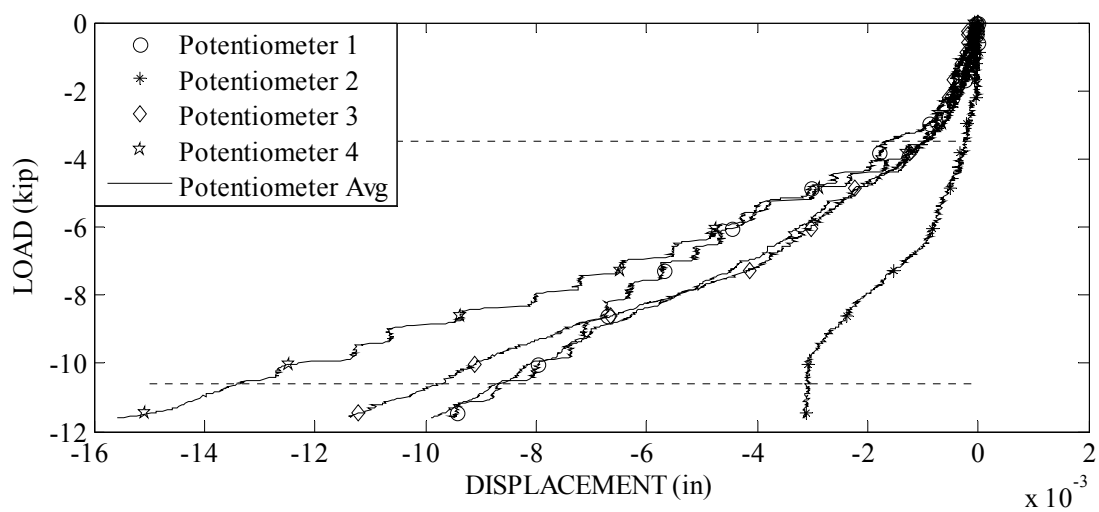

Figure 51 - Load Versus Instrument Deflection, Specimen BC 165, 1-9

R^2, a common measurement of linearity, was indicative of a linear response (.93 to .99), for the slope of the average deflection versus load plots. The number of specimens

This test report shall not be reproduced, except in full, without the written approval of
the AEWC Advanced Structures & Composites Center.

accepted, averaged R^2, elastic modulus, coefficient of variation (COV) of elastic modulus, predicted modulus, and percent difference between predicted and experimental for the 6.50in tubes, are given in Table 18.

This test report shall not be reproduced, except in full, without the written approval of
the AEWC Advanced Structures & Composites Center.

Table 18 Longitudinal Elastic Modulus Properties

Layer Type	**SC 165**	**BC 165**	**DC 165**
Number	25 of 37	8 of 10	10 of 10
E_x **(Kip/in)**	490	454	851
COV %	26.5	15.5	14.2
R^2	0.981	0.993	0.995
Predicted E_x	62.3	65.6	112
% Difference	27.4	17.5	24.9

The relative moduli presented in Table 18 show that the single layer carbon and the single layer carbon with bleeder specimens had close experimental moduli, and they also had close predicted moduli. The bleeder layer has a low relative stiffness compared to carbon fiber or glass fiber and a low fiber volume fraction, estimated at 33% instead of 56% for the other laminae, that gives very little influence to the relative modulus. The increased thickness was offset by decreased stiffness per thickness. The second carbon layer added a significant amount of stiffness to the laminate, about a 40% increase in the relative modulus. The COVs from all three specimen types were high, which suggests that there was a high degree of variability in the stiffness of the specimens or that the gauges did not properly read the deflection. Strain was measured with long gauges that assumed the specimen did not bend during loading. While global bending, the entire cross section shifting out of plane, could be removed from the data, local bending due to material imperfections would not be removed by averaging values. It was not surprising that the single layer specimens, despite a higher number of samples, had a higher COV because they were more prone to local errors as most of their stiffness came from the single carbon layer and any imperfection in that layer would have little support from other portions of the tube. This had a dramatic effect on the buckling strength, but it also loaded the tubes locally and made them more susceptible to producing errors in the gauges.

Predicted modulus was based on Classical Lamination Theory and micromechanics assumptions as detailed in material assumptions. As seen in Table 18, the predictions were not close to the experimental stiffness values. The difference is more likely a reflection on poor measurement technique than a faulty model. A similar version of this model has been compared with just carbon fiber, not a glass/carbon hybrid, and produced errors below 10%, (Bannon, 2009). During testing, the high internal resistance of the displacement gauge made it possible for the gauge to rotate outward instead of compressing, which would have under-measured strain resulting in a stiffness that was too high. In some cases, the measured stiffness was near or below the predicted stiffness,

This test report shall not be reproduced, except in full, without the written approval of
the AEWC Advanced Structures & Composites Center.

but those values were offset by other measured stiffnesses that were more than double the predicted stiffness. The lowest COV of any material during this test was at over 14%, much higher than typical for a composite. This further suggests faulty test practice rather than actual material uncertainty.

Comparison to Models

Several models exist that were compared to the experimental data and used as predictions on the capacity prior to testing. The models poorly predicted the capacity of the laminate because they were formulated for isotropic or orthotropic materials – not anisotropic. Also, the material Poisson's ratio as predicted by micromechanics was 0.3 to 0.53 depending on fiber orientation, but the measured Poisson ratio from mechanical tension testing of a two layer carbon fiber composite, identical to the carbon fiber used in the 11.8in specimens, was 1.26 (Bannon, 2009) and a combined section modulus gives a Poisson ratio of 0.8 to 0.9. All of the models that contain Poisson's ratio broke down if it exceeded 0.5, and those that do not explicitly include Poisson's ratio directly still assume a typical material property of under 0.5. For the purpose of prediction, the micromechanics Poisson's ratio was used instead of the experimental value to give an equation that will produce a real result and does not violate the mechanical principles governing the equation.

Six models are compared with experimental results; all six models were addressed by Kedward (1978), and these models can be divided into two groups of three. The set of models based on compression is from research by Donnell (1934). The other set of models is based on bending research by Brazier (1927). The work by Donnell and Brazier is based on an isotropic material; both models have been modified for both an orthotropic material and an anisotropic layered composite.

Timoshenko (1961) developed this minimum stress value, Equation 6
, for Donnell's defect-based model; Kedward suggested multiplying by 0.606. E is elastic modulus in this isotropic material equation.

$$\sigma_T = \frac{Et}{r\sqrt{3(1-\nu^2)}} \qquad \text{Equation 6}$$

For an anisotropic multilayer composite the previous equation is modified to include the bending stiffness matrix for a composite. This gives increased strength to a material that is stiffer on the outside than the inside; unfortunately this equation was developed for a balanced laminate and tends to be problematic for an unbalanced laminate. In Equation 7 D_{11} is a bending compliance term and Φ, Equation 8

This test report shall not be reproduced, except in full, without the written approval of
the AEWC Advanced Structures & Composites Center.

, is a shear stiffness reduction factor suggested by Kedward; it must be less than one or it is treated as one. Equation 7
is identical to Tatting's (1998) interpretation of the Donnell equation with the additional of a knockdown factor.

$$\sigma_L = \Phi \frac{\sqrt{E_\theta D_{11} t}}{rt} \qquad \text{Equation 7}$$

$$\Phi = \sqrt{\frac{2G_{x\theta}\left(1 - \nu_{x\theta}\nu_{\theta x}\right)}{\sqrt{E_x E_\theta}}} \leq 1.0 \qquad \text{Equation 8}$$

Kedward's orthotropic equation for compression buckling capacity, Equation 9
, is very similar to the anisotropic laminate equation; it replaces the composite stiffness term with its orthotropic value. This equation also clarifies the connection between the orthotropic and anisotropic equations.

$$\sigma_L = \Phi \frac{\sqrt{E_x E_\theta} t}{r\sqrt{3(1-\nu^2)}} \qquad \text{Equation 9}$$

Brazier (1927) used energy methods for a deformable cross section to develop a buckling stress for an isotropic tube. Developed for bending, Equation 10
incorporates internal stress from radius loss.

$$\sigma_B = \frac{2\sqrt{2}}{9} \frac{Et}{\sqrt{(1-\nu^2)}r} \qquad \text{Equation 10}$$

Equation 11
is a modification of Brazier's stress for an anisotropic laminate developed by Kedward. Kedward also provided an orthotropic equivalent in Equation 12
by replacing the bending compliance term with its orthotropic equivalent.

$$\sigma_K = \frac{2\sqrt{2}}{9} \frac{\sqrt{D_{11} E_\theta} t}{tr} \qquad \text{Equation 11}$$

$$\sigma_K = \frac{2\sqrt{2}}{9} \frac{\sqrt{E_x E_\theta} t}{\sqrt{(1-\nu_{x\theta}\nu_{\theta x})}r} \qquad \text{Equation 12}$$

This test report shall not be reproduced, except in full, without the written approval of
the AEWC Advanced Structures & Composites Center.

Using the predicted values for Poisson's ratio, *E*, as well as all of the measured average terms, the experimental local buckling stress was compared to the six local buckling failure predictions.

Table 19 Predicted Compressive Load and Experimental Load in kips

	Bending			**Compression**			
	Isotropic Equation 10	**Orthotropic** Equation 11	**Anisotropic** Equation 12	**Isotropic** Equation 6	**Orthotropic** Equation 7	**Anisotropic** Equation 9	**Experiment**
SC	46.3	36.0	38.0	51.5	52.8	51.0	14.7
BC	72.2	57.3	31.7	80.5	85.0	43.2	23.2
DC	128	76.9	71.7	142	119	104	30.8

No compression prediction comes close to the experimental buckling stress; most over predict capacity by at least 200%. The bending-based predictions do not do much better; with one exception they over predict average compression capacity by at least 100%. Specimens tested had an unbalanced anisotropic laminate – a coupled action reduction was not accounted for in these predictions. Coupled action means that when subjected to axial compression the laminate will want to bend in its principal material directions. Unlike a thin plate, a cylinder has increased rigidity against warping curvatures and it is unlikely the cylinder shape will alter much under the coupling effects, but these expected curvatures will still induce additional stress on the composite not accounted for in any of these models. The importance of coupling can be seen in the predictions for the single carbon and the bleeder carbon buckling stress. The bleeder carbon tube was stronger in experimental tests, it is the single carbon tube with an additional layer to stiffen against out of plane bending, but the model predicts a lower buckling load because the carbon is in the center of two soft materials and therefore cannot contribute much bending resistance, lowering the *D* term versus the single carbon prediction.

This test report shall not be reproduced, except in full, without the written approval of
the AEWC Advanced Structures & Composites Center.

Effect of Known Material Errors on Strength

Materials with the known defects of excessive diameter change and drilled holes have been tested to determine the acceptability of these errors on actual bridges.

Diameter Inconsistency

Diameter inconsistency is a problem that to a certain extent every arch suffers from. During the manufacture process the diameter of the inflated e-glass braid was measured at use angle, and while it is typically close to the nominal values, there are always fluctuations at the several hundredths of an inch level. Change in diameter could have a severe impact on the strength performance of an arch. Inconsistent diameter implies a region where the material has a tapered shape and loads traveling though the wall thickness are partially directed away from the vertical axis of the arch. The stiffness of the arch through the wall thickness direction was several orders of magnitude lower than the longitudinal or radial stiffness. Even small loads directed through the thickness result in shape changes leading to buckling instability. Buckling was more of an irrecoverable shape change than fiber failure, and shape change was exacerbated by initial diameter irregularities.

Specimen Description

In all arches, the inner E-glass braid layer holds the diameter of the arch constant during resin infusion. The imperfections in this layer varied the diameter of the circular cross section or made the section less circular. The fabric reinforcement typically has slight changes in diameter, but they are acceptably small and gradual, less than 1% total change over the specimen (not readily visible). Diameter fluctuations are measured as change in the perimeter of the inflated E-glass braid layer measured with a pi tape or a cloth tape at 6.0in intervals. Measurements were made at the E-glass braid placement stage of fabrication to avoid resin ridges that are formed during infusion. The manufactured tube had no sudden bulge or hourglass deformities that developed in less than 6.0in; the measuring method did not entirely miss any diameter defects, although local maximum and minimum diameters of the varying diameter wave were not necessarily measured. An eccentricity term was created to quantify inconsistent perimeter, this term is the percent change in perimeter in a 6.0in interval Equation 13

.

$$\text{eccentricty} = \frac{\Delta D}{6.0in} \qquad \text{Equation 13}$$

A gradual taper over the full 24.0in height of a specimen would have a lower eccentricity than a specimen with no taper over 18.0in of the height and a steeper taper over the final 6.0in.

This test report shall not be reproduced, except in full, without the written approval of the AEWC Advanced Structures & Composites Center.

This test report shall not be reproduced, except in full, without the written approval of
the AEWC Advanced Structures & Composites Center.

Table 20**Error! Reference source not found.** contains the measured diameter and the calculated eccentricity for all of the control and inconsistent diameter specimens (ID). An eccentricity of two-thirds of a percent (0.67%) was a threshold for diameter inconsistency, and a specimen from each group was very close to this threshold. Visual observation was very important in this process; all of the inconsistent diameter tubes were taken from a length of tube that looked wavy; specimen SC 300-6 was also taken from this section but measured with such low eccentricity it was included with the control specimens.

This test report shall not be reproduced, except in full, without the written approval of
the AEWC Advanced Structures & Composites Center.

Table 20 Diameter Measurement for Inconsistent Diameter Specimens

Sample	Top D (in)	Mid 1 D (in)	Mid 2 D (in)	Bottom D (in)	Eccentricity %
SC 300-1	11.7	11.7	11.6	11.7	0.439
SC 300-2	11.7	11.7	11.7	11.7	0.169
SC 300-3	11.7	11.7	11.7	11.7	0.169
SC 300-4	11.7	11.6	11.6	11.6	0.509
SC 300-5	11.6	11.7	11.8	11.7	0.644
SC 300-6	11.6	11.6	11.6	11.6	0.272
SC 300-ID-1	11.6	11.6	11.6	11.8	1.22
SC 300-ID-2	11.8	11.8	11.6	11.6	1.81
SC 300-ID-3	11.6	11.6	11.6	11.7	0.883
SC 300-ID-4	11.7	11.8	11.5	11.8	2.08
SC 300-ID-5	11.8	11.8	11.7	11.6	0.969
SC 300-ID-6	11.6	11.6	11.7	11.8	0.678
SC 300-ID-7	11.8	11.8	11.8	12.0	1.70

A piece of e-glass that had been rejected from manufacturing due to visible diameter flux was used to manufacture 11.8in specimens. The capacity of the visibly bad specimens was compared with those from the same tube that had little diameter variation and some tubes with bleeder material. Sample sizes were small as all three groups of tubes were taken from the same long specimen.

Results

There was a large difference between the normal, inconsistent diameter, and bleeder-covered specimens, in Table 21.

Table 21 11.8in Specimen Ultimate Strength

Specimen	SC 300	SC 300-ID	BC 300
Ultimate Load (Kip)	19.9	13.8	29.0
COV	18.5	5.80	17.4
Sudden Buckles	3 of 6	0 of 7	2 of 5

The additional bleeder layer caused a considerably higher capacity, approximately 50%, while inconsistent diameter fabric showed 30% lower strength. Having multiple failure rates caused the high COVs of the normal and bleeder specimens. Normal and bleeder specimens each had some specimens fail with higher than average loads in a sudden

This test report shall not be reproduced, except in full, without the written approval of
the AEWC Advanced Structures & Composites Center.

buckling mode. The other specimens, including all of the inconsistent diameter specimens, failed in progressive slow failure modes. Boundary conditions are a potential source of this difference as the same plywood end caps were used for every specimen and they became heavily grooved by the end of testing. However, the high COV and the difference between sudden and progressive buckling were also true for the 6.50in specimens that were tested with new boundaries on every specimen. Ineffective deflection measurements were taken from these specimens so any attempt at calculating elastic modulus was inaccurate and it was impossible to judge the evenness of the stress distribution around the entire perimeter from only two points.

Concrete Filling Holes

Arches are field filled with concrete and the concrete must have a means of entering the arch. Two methods, end filling and crown filling, have been employed and are discussed in Walton (2011). Crown filled arches require a 2.52in -2.95in hole to be drilled in the arch for the concrete pipe to gain access. This hole at the crown of the arch was in a high bending stress region – in an area that was in the compression face of the arch.

Holes have a detrimental effect on composite materials and researchers have tried to quantify the effect of holes in various composite materials. Saha (2004) tested pultruded e-glass fiber with polyester matrix plates with a series of holes ranging from 7% to 69% of the width. Results showed a reduction in capacity of 66%-70% from the smallest hole to the largest hole depending on specimen thickness, with thinner specimens achieving higher compressive stress capacities. Similar reductions have been found in carbon fiber composites (Rhodes and Mikulas, 1987).

Soutis and Fleck (1990) tested graphitic carbon fiber composites in compression with mixed fiber angles (+/-45 degree and 0 degree) and holes. Specimens were 1.97in wide with 0.197in diameter holes. The average failure stress of specimens with holes was 45% lower than specimens without holes. During compression failure, specimens failed initially at the 0 degree plies; high relative stiffness attracted much of the load. Similar results have been found by other researchers (Arslan, 2009). Failure in tests by Arslan were consistent: all specimens failed within 5% of the same load, failed near the hole, and failed at a lower load than all specimens without holes. The author concluded that the consistent failure mode and load were indicative of a failure controlled by the hole.

<u>Holes in 14.4in Specimens</u>

The effect of a hole on capacity was explored in two series of testing. First, eight total 14.4in diameter specimens were tested in axial compression. These specimens had four control specimens without holes and four specimens with 2.95in -4.15in holes drilled at the middle of their 29.9in height. Specimens were cut apart with a horizontal band saw

This test report shall not be reproduced, except in full, without the written approval of
the AEWC Advanced Structures & Composites Center.

that was too small to cut the specimens in a single pass causing the specimens to have a large variation in height and a visibly uneven edge. Instrumentation was mounted as described for the 6.50in specimens only the gauge length was increased to 22.4in. Load rate for this test was 0.2in/minute. Figure 52 shows a comparison of tests performed on 14.76in diameter specimens with and without a hole to show the scale of the hole relative to the specimen.

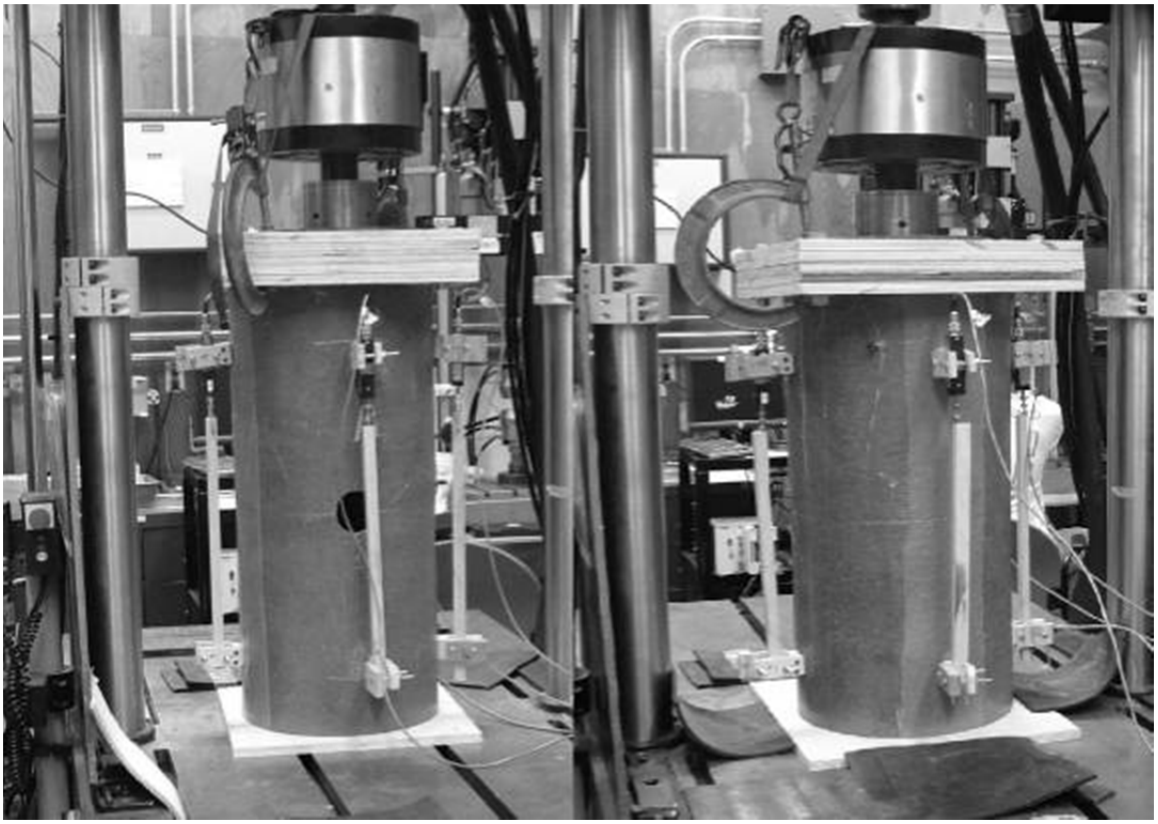

Figure 52 - Compression Test, 14.76in Diameter, With Hole and Without Hole

Specimens with holes had a lower load capacity than specimens without holes, but the difference between the specimens was clouded by the edge imperfections from the cutting process. In the case of some tests there was a load of 9kip on the specimen while there was still a visible gap between the specimen and the plate – half of the ultimate load was applied before the second side saw any load.

Table 22 contains a comparison between the loads of the two specimen types.

Table 22 Ultimate Load on 14.76in Tubes

This test report shall not be reproduced, except in full, without the written approval of
the AEWC Advanced Structures & Composites Center.

Type	Control	Hole
Failure Load (Kip)	31.9	19.4
COV %	17	30.4

The holes created a loss in load capacity of 40% compared to specimens without holes. This value may be artificially low due to the irregular boundary conditions. The uneven end cuts would have a more detrimental effect for the control specimens because they did not have a controlling defect. Buckling failures were precipitated by defects, and all control specimens had a preexisting boundary defect while all specimens with holes had the hole as a primary defect. All four of the specimens with holes buckled at the hole, meaning that the hole was a larger defect than the unevenness at the end points. For some of the specimens with holes it was possible that the uneven boundaries improved the capacity because stress concentrations were directed away from the known weak spot until the tube was sufficiently loaded to damage the plywood end caps and begin loading the holed section, while an even load distribution would have already compromised the hole. Control specimens could only be hurt by stress concentrations at any location because their nominally equal strength around the circumference gave no preferential failure location.

Holes in 6.50in Specimens

Holes were also drilled in a series of 6.50in diameter, 15.0in length, double carbon and bleeder carbon specimens. Identical material and specimen dimensions to prior 6.50in diameter cylinders, these cylinders had holes drilled at mid height. All bleeder carbon specimens had a 1.75in diameter circular hole drilled at the mid height. Nine of the double carbon specimens had the same 1.75in hole and eight specimens had a larger 2.95in -3.15in hole. All holes were cut with a hole saw. The smaller hole was picked as the closest hole saw size equivalent (ratio of diameters) to a 3.0in hole in a 11.8in specimen, a typical case for filling. The larger hole size for double carbon specimens did not reflect a real world application; it served as a hole substantially larger than the 1.75in hole and a second data point for comparison with the finite-element models discussed in the section modeling buckling for a hollow cylinder. Strain was not measured during testing. Figure 53 shows the specimens with holes during tests.

This test report shall not be reproduced, except in full, without the written approval of
the AEWC Advanced Structures & Composites Center.

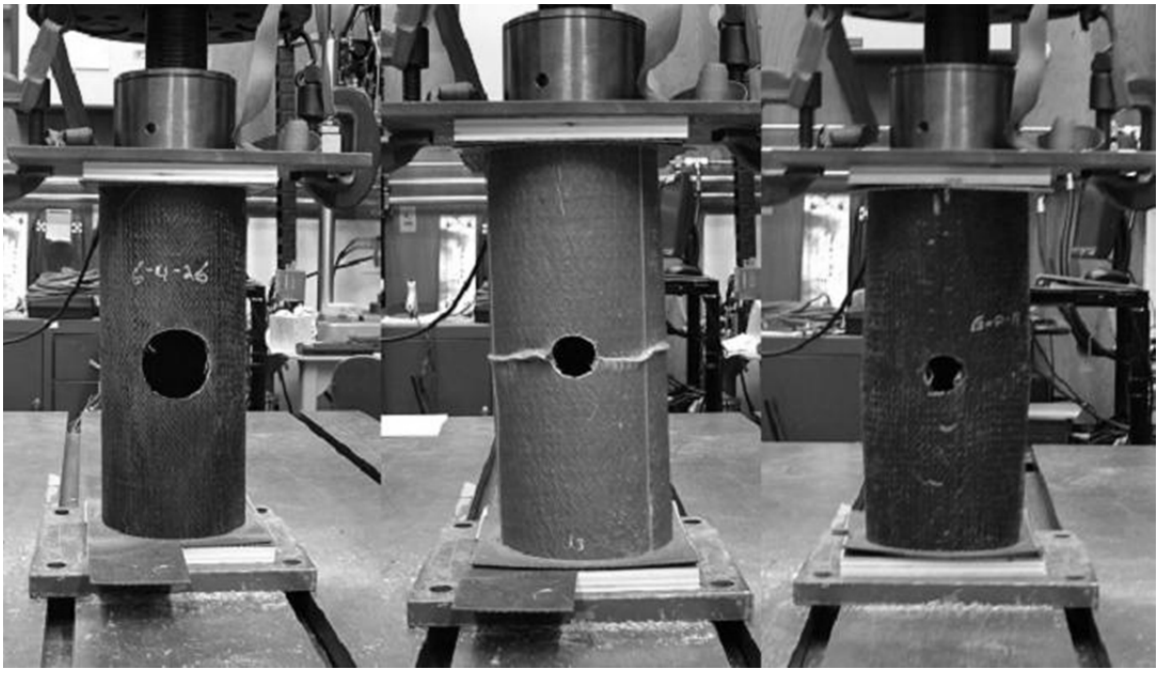

Figure 53 - DC 165-76, BC 165-45, and DC 165-45

Results for specimens with holes are in Table 23, for comparison, specimens without holes are in Table 17. Drilling holes significantly lowered the buckling capacity compared to cylinders without holes; a 1.75in hole reduced the capacity of bleeder carbon specimens by 51% and double carbon specimens by 46%. The strength drop for a specimen with a hole is large enough that special consideration should be taken for design of the apex of an arch. It is possible that it would be unconservative to design an arch based on the highest stress during filling, which generally occurs at the footing or the shoulder, and the strength of a cylinder without a hole.

FRP topped plywood end caps were used for all specimens with holes. This boundary type performed best out of all tested boundaries, but to generate an even load distribution in specimens with irregular edges, the plywood needed to crush around the cylinder prior to specimen buckling. Specimens that buckled before plywood crushing were not accepted as part of the mean or the COV because they had most likely loaded unevenly and failed around the hole at a local stress not indicative of the total load in the specimen. Plywood crushing was obvious from the sound it made during a test; the typical load for plywood crushing was 5.85kip-7.87kip; all specimens excluded failed below 7.87kip. The COV, after ignoring the low specimens, was low compared to prior results for specimens without holes and typical local buckling testing. Single carbon and bleeder carbon specimens without holes both had a buckling capacity COV over 15%. Donnell

This test report shall not be reproduced, except in full, without the written approval of
the AEWC Advanced Structures & Composites Center.

(1934) tested common thin-walled metal cylinders made from brass, steel, and aluminum and found that buckling capacity COV was greater than 20% for isotropic, uniform metals, because even small deformities in the shell (on the order of the thickness) could result in substantially reduced buckling capacity, and these deformities could not be removed during manufacture. Low COVs are indicative of a failure dominated by a single uniform defect that is consistent for every specimen in the group, instead of being dominated by random imperfections. The effect of a sizeable hole is larger than the diameter inconsistencies in typical cylinders, and as such it dominates the failure response.

Table 23 Results of 6.50in Specimens with Holes

TYPE	Load (kip)	COV %	# Tested	# Accepted
Bleeder Carbon	11.1	7.8	14	11
Double Carbon (Small)	16.7	5.7	9	9
Double Carbon (Large)	10.7	7.5	8	7

Summary

Arches experience construction loads before concrete hardens, and at this time they rely only on the strength of the composite shell. The capacity for a section in axial compression is expected to be nearly equivalent to the capacity of the section in bending because both failures are precipitated by buckling of the compression face. Existing analytical models do a poor job of predicting this local compressive buckling of the composite tubes because of the extreme thinness of the tube, the large Poisson ratio from braid interaction, and the inability of the models to fully capture the complex fiber architecture of the tube. To establish the relative accuracy of these models and get baseline data for future modeling and immediate bridge safety, short specimens were tested in axial compression. These specimens had a variety of diameters and used one or two layers of carbon for the longitudinal reinforcing or bleeder as an abrasion layer over a layer of carbon. Two layers of carbon doubled the strength of the composite compared to one layer since it increased axial stiffness and thickness (which enhances radial stiffness), and bridged gaps in the first carbon layer. The bleeder layer gave a 50% increase in capacity without adding axial stiffness by increasing the thickness (thus enhancing radial stiffness) and bridging holes in the carbon. When filling an arch with concrete it has been necessary to cut holes in the composite. Preliminary testing indicates at least a 40% loss in axial capacity due to a 2.95in diameter hole in a 14.8in diameter carbon bleeder tube.

This test report shall not be reproduced, except in full, without the written approval of
the AEWC Advanced Structures & Composites Center.

MODELING BUCKLING FOR A HOLLOW CYLINDER

Due to the poor compressive buckling capacity estimates of many of the analytical models discussed in the section compression of hollow FRP – and the inability of these models to predict the effect of drilling a hole in the composite and other geometric irregularities – a finite element model was constructed to help understand the results from the structural compressive testing. Abaqus Standard (Dassault Systemes, 2010) was used as the modeling platform. Models of the composite tubes were built based on the three 6.50in diameter, 15.0in long specimen lay-ups tested in axial compression as detailed in the last section. This section covers the element type selection, material characterization, and level of mesh refinement using linear elastic (eigenvalue) buckling analysis. Models were then constructed to study the effect of unbalanced loading and geometric imperfections on buckling capacity. Finite-element models of the composite cylinder were then constructed with a hole added at mid-height to simulate the concrete filling port, and the effect of the hole on compressive capacity is examined.

Selecting Analysis Parameters – Eigenvalue Buckling Analysis

The cylinder was modeled using shell elements. The cylindrical shell was restrained from out of plane motion and loaded by a constant shell edge load. Figure 54 shows load and boundary conditions for a cylinder. Edge displacements are restricted in x- and y-axes, edge rotations are restricted about the z-axis and load is applied normal to the circular ring surface of the cylinder (z-axis for an unperturbed cylinder).

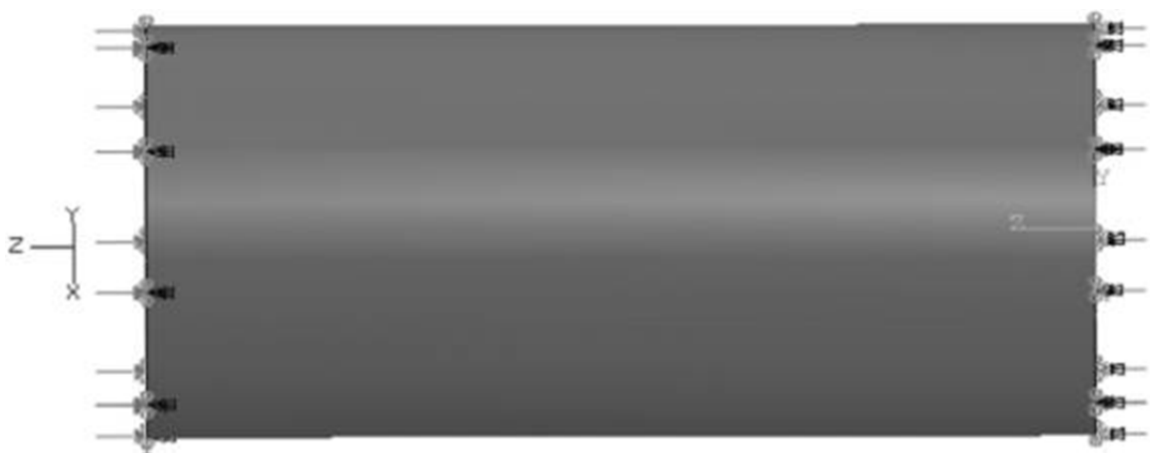

Figure 54 - Load and Boundary Conditions for a Typical Cylinder Model

This test report shall not be reproduced, except in full, without the written approval of
the AEWC Advanced Structures & Composites Center.

In an eigenvalue buckling analysis, the eigenvalue is the number that when multiplied by the applied load gives the buckling load. Instead of reporting the eigenvalue, the buckling load (in kips) is reported for easier comparison with the experimental results.

According to the Abaqus users manual (Dassault Systemes 2009), there are three elements (S4, S4R and the S9R5) that work well for shell buckling. The S9R5 element is a quadratic element with an intermediate node on each side and a central node that uses reduced integration through the depth. This element assumes thin shell behavior, which is consistent with the radius to shell thickness seen in the experimental tubes, but it cannot be selected from the Abaqus graphical user interface (GUI), making it cumbersome to use. The S4R element is a linear element (nodes only on the corners) with reduced integration. It requires a finer mesh than the quadratic element for the same level of accuracy, but reduced integration helps the run time. The S4R element is prone to hourglassing, sometimes producing fictitious buckling modes (Dassault Systemes, 2009). The S4 element results in models with longer run times for the same level of accuracy when compared with the other elements because it is linear and does not have reduced integration. However, the S4 element is an all-purpose shell element and is not prone to false buckling modes. Ultimately, the S4 element was selected for this study.

Selecting Material Properties

After choosing the S4 element type, the next step was to select a material model to best mimic the shell wall for the three types of 6.50in diameter tube lay-ups. In the Section Mesh Refinement, the best mesh density, which has 7650 equal size elements, is determined, and all analyses in this section rely on that mesh. For all models, the thickness was 0.035in for the e-glass layer, 0.027in for carbon, and 0.029in for the bleeder layer. These values reflect the measured thickness of the shell wall as seen in Chapter 2 on compression testing. All material models use predicted elastic properties, since insufficient experimental results exist for the exact fiber lay-up. See Material Assumptions for Classical Lamination Theory material assumptions.

<u>Isotropic</u>

The simplest material model, isotropic, assumes that the material has the same properties in every direction and requires only the elastic modulus and Poisson's ratio for inputs. Some buckling models (Brazier 1927 and Timoshenko 1935, 1961) assume uniform material properties. The tubes have different elastic moduli in the longitudinal and radial direction; the balanced modulus in Table 24 was taken as the square root of the multiple of the longitudinal and radial moduli, Equation 14. This approach is similar to the orthotropic buckling models in the comparison to models section that utilize the square

This test report shall not be reproduced, except in full, without the written approval of
the AEWC Advanced Structures & Composites Center.

root of both principal moduli, compromising between the difference in longitudinal and radial elastic modulus.

Table 24 Material Properties for Isotropic and Engineering Constant Models

Title	S C	B C	D C
E_x (Ksi)	5740	4080	7180
E_θ (Ksi)	3650	2670	3050
$E_{balance}$ (Ksi)	4580	3290	4680
V_{12}	0.335	0.338	0.476
G_{xy} (Ksi)	1330	979	1610

$$E_{bal} = \sqrt{E_x E_\theta}$$

Equation 14

Poisson's ratio for the longitudinal, radial direction was used as the Poisson's ratio for the entire material. This model should not be a good prediction of the buckling strength and if the longitudinal elastic modulus were used for E_{bal}, the result would serve as an upper bound for the buckling capacity. This model predicts the same buckling pattern for all three models, Figure 55, which does not accurately reflect the double carbon specimens' tendency to buckle near the boundary. Table 25 gives the buckling capacity for each of the four models tested with each material type.

Table 25 Buckling Capacity of Material Models

Material Models	Isotropic	Orthotropic	1-Layer	2-Layer	Experimental
SC	243	236	162	153	68.7
DC	601	548	372	304	138
BC	417	390	210	197	101

This test report shall not be reproduced, except in full, without the written approval of the AEWC Advanced Structures & Composites Center.

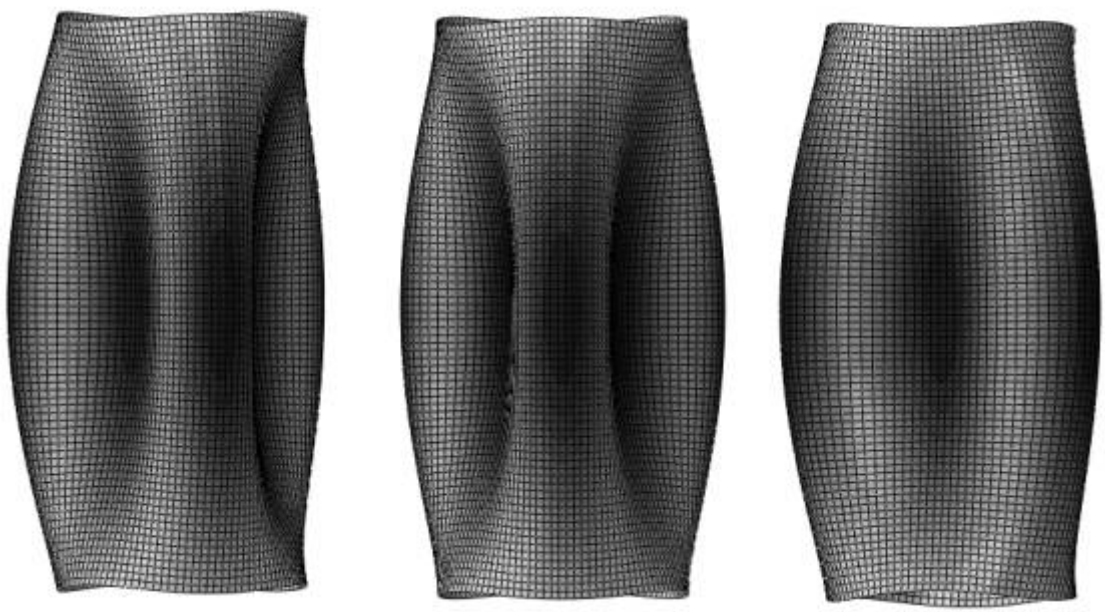

Figure 55 - Isotropic Model Single Carbon, Double Carbon, and Bleeder Carbon

Engineering Constant – Orthotropic

The engineering constant model allows moduli to be specified in orthotropic directions. Material properties are constant through the thickness, but the longitudinal moduli give a higher longitudinal stiffness and a lower transverse stiffness versus the isotropic model.

contains the independent properties for this material model, which were generated using Classical Lamination Theory. This model predicts different buckling shapes for each material model, and these shapes may reflect experimental results. As in Figure 56, double carbon specimens had a strong tendency to buckle near the support, and the model predicts buckling away from mid height. Also, the single carbon specimen shows a tendency to buckle at mid height. However, the response of the bleeder carbon and double carbon specimens was not identical as predicted by Figure 56. Double carbon specimens were more affected by edge buckling than bleeder carbon specimens and this was not reflected by the orthotropic model. The first two models assumed uniform properties through the cross section, and both models poorly predict load or buckled shape.

This test report shall not be reproduced, except in full, without the written approval of
the AEWC Advanced Structures & Composites Center.

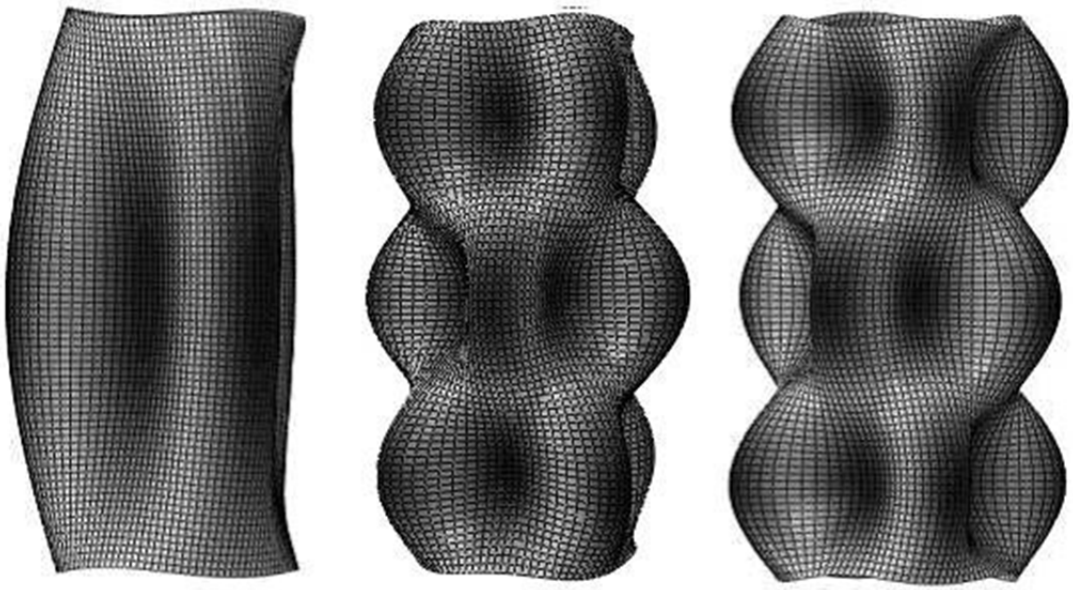

Figure 56 - Orthotropic Single Carbon, Double Carbon, Bleeder Carbon

Lamina with Two Layers per Braid

A braided layer is often treated as separate consecutive opposing layers (Bannon 2009). For this model, lamina material values were used with the micromechanics values for the 1, 2, and 3 material axes as in Table 26. In the Abaqus composite material editor, the materials were set to their appropriate angle (+/- 81 for the e-glass and +/- 22 for the carbon fiber). Abaqus calculated the final stiffness in the cylinder's longitudinal, radial and transverse directions during the solution phase. For this material model (and the one layer per braid material model described in the next section), the bleeder material is modeled as an isotropic layer with uniform properties in each direction. It is then added as an additional layer in the material model angled at 0 degrees. This model predicts a torsional mode for tube buckling as shown in Figure 57, which was not experimentally observed. Laminate composite modeling performed by Weaver (2002) shows a similar torsional buckle using a symmetric laminate based on coupled bend/torsion. Weaver's model showed a 30% reduction from a torsional buckling mode that could be avoided by using a different laminate schedule that minimizes flexure/torsion coupling. Both laminate schedules proposed by Weaver (2002) had the same classic buckling loads using analytic models. In this material model torsional buckling comes from the stacking of the carbon laminates, an outer layer 22 degrees and an inner layer of oriented at -22 degrees. The tube becomes stronger in the 22-degree direction because it is further from the neutral axis and adds higher bending resistance, allowing the tube to buckle in the opposite direction. In an actual braid the +22 and –22 layers interact and both affect the

This test report shall not be reproduced, except in full, without the written approval of
the AEWC Advanced Structures & Composites Center.

full thickness of the carbon layer, so torsional buckling should not occur for a braided composite.

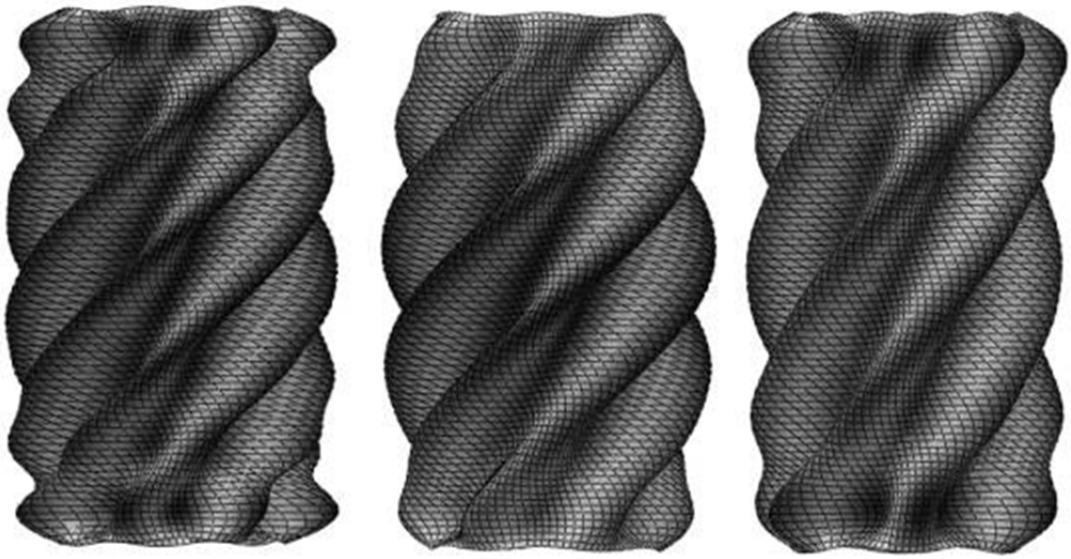

Figure 57 - 2-Layer/Braid Model Single Carbon, Double Carbon, Bleeder Carbon

Table 26 Properties for Lamina 2-Layers

Property	**Carbon**	**E-Glass**	**Bleeder**
E_1 **(Ksi)**	15500	5420	711
E_2 **(Ksi)**	1900	1670	711
ν_{12}	0.266	0.283	0.334
G_{12} **(Ksi)**	434	437	225

Lamina with One Orthotropic Layer per Braid

In this approach each braided composite layer was treated as a single orthotropic layer in the Abaqus composite editor. A micromechanics worksheet was created to calculate the stiffness, shear stiffness, and Poisson's ratio of each layer treating it as a two-layer composite with opposite directional plies that occupy the same space (+/-22 degrees for the carbon, +/-81 degrees for the e-glass). These properties, in Table 27, were entered into a lamina material model in Abaqus for each material. The e-glass and carbon braid properties were stacked in the Abaqus composite editor and positioned at 0 degrees, because the angular direction was already accounted for by the reported material

This test report shall not be reproduced, except in full, without the written approval of
the AEWC Advanced Structures & Composites Center.

properties. This model had a simple adjustment between single carbon, double carbon, and bleeder carbon tubes where only an additional layer needed to be added or subtracted using the Abaqus composite editor.

This model consistently produced the most reasonable buckling shapes based on comparisons with the experimental data. For the single carbon and carbon bleeder specimens the tube is predicted to buckle at mid span as shown in Figure 58, which is consistent with experimental results where a majority of specimens broke away from the support. Double carbon models buckle in five half-sine waves over the height of the model. This buckled shape has a maximum deformation close to the edge of the tube, and 90% of the experiments on double-carbon tubes exhibited end failures.

Table 27 Engineering Constant Properties 1-Layer

Property	**Carbon**	**E-Glass**
E_x **(Ksi)**	9530	1640
E_y **(Ksi)**	1650	5160
ν_{xy}	1.085	0.109
G_{xy} **(Ksi)**	2260	608

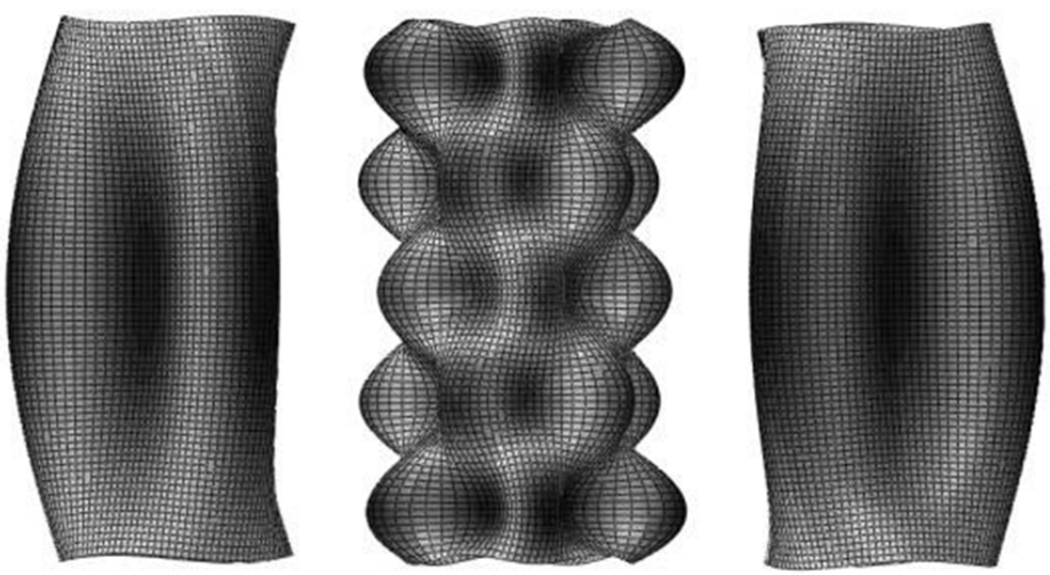

Figure 58 - 1-Layer/Braid Model Single Carbon, Double Carbon, Carbon Bleeder

This test report shall not be reproduced, except in full, without the written approval of
the AEWC Advanced Structures & Composites Center.

Mesh Refinement

After deciding on the 1-layer per braid material model, a mesh refinement study was performed on all three material types to determine the mesh density required to produce an accurate buckled shape and buckling load. All meshes were uniform with equal-sized elements. The total number of elements ranged 300 for the coarsest mesh to over 47000 elements in the finest mesh. In all cases the element was selected to be a quadrilateral and ABAQUS defaults to make all elements as close to square as possible for a given geometry; for a cylinder all elements were square because there were no irregularities for ABAQUS to have trouble meshing. The number of elements has a substantial impact on computation time and solution accuracy. The best element size converges to a consistently accurate solution in an acceptable time, since the large matrix of analyses run in this modeling program prohibits a very high degree of mesh density. 7650 elements, corresponding to an element edge length of 0.197in, were used for all additional modeling. The 7650 element mesh averages 1 minute per buckling solution, the 18055 element mesh averages 8 minutes per buckling solution; the improvement in computation time is worth the sacrifice in computation accuracy, shown in Table 28. Percent change in Table 28 is the change relative to the finest mesh.

This test report shall not be reproduced, except in full, without the written approval of
the AEWC Advanced Structures & Composites Center.

Table 28 Mesh Refinement Study

Number of Elements	Percent Change	Load (Kip)
Single Carbon		
300	18.1	42.9
1887	2.87	37.4
3942	1.38	36.9
7650	0.387	36.6
18055	0.213	36.4
30200	0.0672	36.4
47685	-	36.4
Bleeder Carbon		
300	18.8	56.4
1887	3.03	49.0
3942	1.47	48.3
7650	0.932	47.2
18055	0.460	47.7
30200	0.077	47.4
47685	-	47.4
Double Carbon		
300	24.2	103
1887	6.91	88.3
3942	3.69	85.7
7650	1.29	83.6
18055	0.672	83.2
30200	0.178	82.5
47685	-	82.7

This test report shall not be reproduced, except in full, without the written approval of
the AEWC Advanced Structures & Composites Center.

Experimental Imperfections

The eigenvalues predicted by the different material models are considerably higher than the experimentally observed buckling loads. However, all models have thus far assumed a perfect cylinder loaded by a perfectly concentric load. No fabricated tube is a perfect cylinder, and manufacturing imperfections create diameter changes and curvatures over the length. Also, in many tests the load was eccentric, as seen from the potentiometer data reported in compression of hollow FRP. Therefore, applying a uniform load does not accurately reflect the load seen by many specimens. To see the effect of these two inconsistencies on the buckling capacity, modified models were constructed using the uniform mesh with 7650 elements selected in the mesh density study and using one orthotropic layer per fabric layer to model the composite shell wall. Other imperfections that will not be covered are local variations in thickness, stiffness, and waviness.

Effect of Unbalanced Loading

Two different unbalanced loads were applied to the tube: one where the load varies linearly from 0 to double the average load across the cylinder diameter, and a second case where the load varies linearly from 2/3 of the average load to 4/3 of the average load across the cylinder diameter. The first unbalanced load represented the case where one side of the cylinder is entirely unloaded while the second case was for a cylinder where there was some load everywhere – a more moderate loading case. Table 29 displays the predicted buckling capacity of cylinders subjected to unbalanced load. Capacity was slightly reduced by the moderate unbalanced load: the bleeder carbon model reduced by only 1.5% and the double carbon model by 9.1%. The higher unbalanced load produced a 28% to 33% reduction in capacity that brings the buckling load closer to the experimentally observed values. The experimental buckling load was still considerably lower than the model-predicted buckling load, however. Further, many specimens did not show evidence of eccentric load; plywood loading platens deformed based on load reducing eccentricity from uneven edges. Other defects must also contribute to the discrepancy between experimental and modeled buckling load.

Table 29 Capacity of Cylinders with Unbalanced Loads

TYPE	SC	BC	DC
Regular	162	210	372
Moderate Unbalance	150	207	337
Full Unbalance	109	152	249

This test report shall not be reproduced, except in full, without the written approval of the AEWC Advanced Structures & Composites Center.

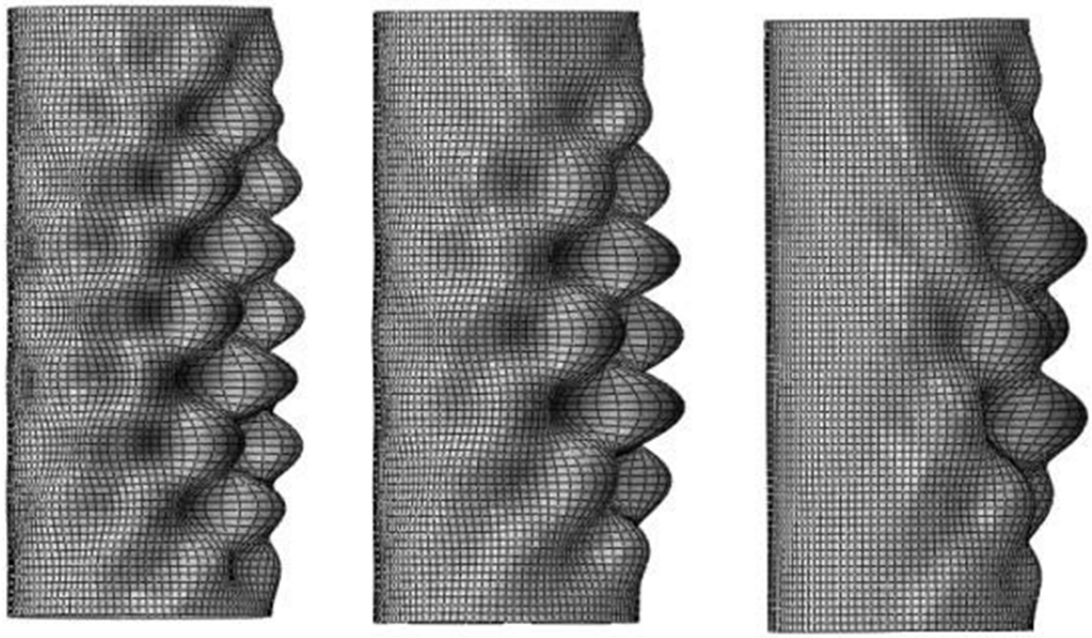

Figure 59 - Uneven Load Models Single Carbon, Double Carbon, Bleeder Carbon

Effect of Geometric Imperfections

Geometric irregularity is a consequence of manufacturing that was present in the tested specimens. The cylinder used for mesh refinement and material model determination was a perfect cylinder and was not indicative of experimental specimens. Here, geometric imperfections that affected the full geometry of the cylinder are considered, such as cross sectional diameter variation and longitudinal curvature. Local, node-level variations in thickness and stiffness were ignored, however they also potentially affected experimentally determined buckling capacities.

The initial perfect cylinder model was created in the Abaqus GUI. Abaqus generates an input file from its GUI and then loads this file in the 'job' module when running an analysis; Abaqus can also load an input file directly without a model. The input file contains the nodal connections, coordinates, and lay-up scheme for each part as well as the global material properties, boundaries, loads, and part interactions. To perturb the mesh into an irregular geometry, only the nodal locations needed to be modified – connections and material properties remain constant. A MATLAB routine was written to modify the nodal coordinates into a variety of shapes keeping all of the boundary and connectivity information constant (see Walton (2011) for this code). The MATLAB routine has five inputs: lay-up, hole size (see eigenvalue buckling analysis of tubes with

This test report shall not be reproduced, except in full, without the written approval of
the AEWC Advanced Structures & Composites Center.

holes), perturbation type, scale, and extra – a way of altering the perturbation type for models with holes (see effect of geometric imperfections in tubes with holes).

Table 30 contains the buckling loads calculated from the Abaqus eigenvalues for the cylinders with a variety of defects. Defects are explained in subsequent sections. Defects range from the double-carbon 0.10in arc perturbation with a 14% increase in capacity to the single carbon, single curvature perturbation with a reduction in capacity of 61%. As discussed in the following sections, the size of the defects falls within the range of actual defects that were measured in the test specimens.

Table 30 Strength of Cylinders with Geometric Imperfections

Deformation Type	SC	DC	BC
Non-Deformed	163	372	210
Hourglass - 0.02in	148	369	192
Hourglass - 0.06in	122	322	161
Hourglass - 0.10in	101	281	135
Bulge - 0.02in	169	371	220
Bulge - 0.06in	166	366	215
Bulge - 0.10in	161	357	210
Single Curvature - 0.10in	148	351	192
Single Curvature – 0.30in	96.1	245	129
Single Curvature – 0.50in	63.4	171	86.9
Double Curvature - 0.10in	151	366	196
Double Curvature - 0.06in	120	311	161
Double Curvature - 0.50in	94.9	260	131
Ellipse - 0.10in	162	369	209
Ellipse - 0.06in	153	345	200
Ellipse - 0.50in	135	310	178
Arc - 0.10in	181	424	225
Arc - 0.06in	114	291	149
Arc – 0.50in	72.0	198	98.0

Inconsistent Diameter

The laboratory specimens exhibited a small but measurable amount of diameter inconsistency. Most specimens varied in perimeter from 20.2in to 20.6in (over the full ~11m length of the infused part). The local variation in the part (over the 15.0in specimen height) was usually small, but 0.03in changes in diameter were measured in nearly every specimen, and 0.08in or larger changes in diameter (over 0.24in changes in

This test report shall not be reproduced, except in full, without the written approval of the AEWC Advanced Structures & Composites Center.

perimeter) from top to mid height or mid height to bottom were measured in ~25% of specimens, and there is a rough correlation between diameter change and buckling capacity, discussed in diameter inconsistency. Diameter variation was caused by inconsistency in the glass diameter constraint layer, or over-tensioned carbon fiber restricting the diameter of the tube. Models were created to reflect these diameter inconsistencies in the specimen. This took on three different forms: hourglass shape (diameter contraction in the middle), bulge (diameter expansion in the middle), and ellipse (cross section has a minor radius and a major radius).

Hourglass

The hourglass shape was a uniform and symmetric reduction in diameter. Diameter loss was based on the height of the cylinder varying along a sine wave with period equal to the height of the cylinder and amplitude equal to variable *scale*. The peak of the sine wave occurs at the ends of the tube and the trough of the wave occurs at mid height making the mid height the smallest diameter. Any sharp discontinuities in diameter present in actual specimens are visible during manufacture, and such specimens are rejected, so the smoothed shape of the sine wave was assumed to be a reasonable representation of the diameter variation in an actual cylinder. The equation for the diameter change, Equation 15, depends only on nodal height *Z*.

$$radius_change = \frac{-\sin\left(\left(Z - \frac{Z_{\max}}{4}\right)\left(\frac{2\pi}{Z_{\max}}\right)\right)}{2} * scale \qquad \text{Equation 15}$$

After calculating diameter change, the new diameter at each node was converted back into rectangular coordinates. Figure 60 contains a wire mesh plot of the deformed nodal locations before buckling analysis. Note that this shape has an extreme degree of hourglass – ten times the maximum used in analysis – and is a graphical representation, not actual input coordinates.

This test report shall not be reproduced, except in full, without the written approval of the AEWC Advanced Structures & Composites Center.

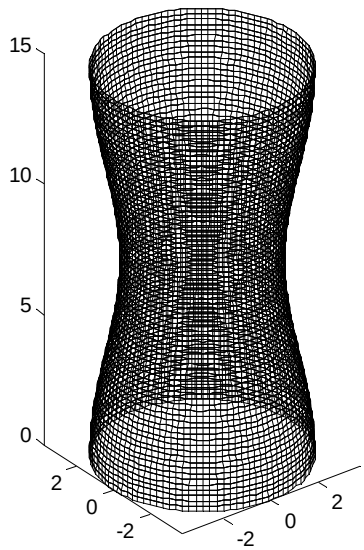

Figure 60 - Wire mesh of hourglass perturbation, 0.984in radial decrease at center

Buckling capacity was greatly affected by this perturbation, but the buckled shape remained the same for many cases. Table 30 contains the buckling capacity for cylinders without holes and with geometric irregularities. With a 3.08% loss in diameter, the model experienced a 24% to 38% loss in capacity depending on lay-up. The single carbon and carbon bleeder models have no appreciable shape change with any of the three hourglass shapes tested or the initial perfect cylinders. The double carbon model with the lowest degree of hourglass tested (0.02in) retained the buckled shape of the perfect double carbon cylinder, as in the left of Figure 61. The middle and highest values of hourglass deformation modified the buckled shape into the center-buckled shape shown in the right of Figure 61. Measured levels of diameter variation over the length of most specimens fell between the perfect cylinder and the lowest hourglass shape (or bulge shape) and from the perfect shape to the 0.02in contraction there was no change in buckled shape. The different buckled shape of the more irregular double carbon cylinders indicates that moderate hourglass may have contributed to the one of ten double carbon specimens that broke at its center. However, the specimen that broke at its center had a higher buckling load than any other double carbon specimen making it unlikely to be caused by an imperfection.

This test report shall not be reproduced, except in full, without the written approval of
the AEWC Advanced Structures & Composites Center.

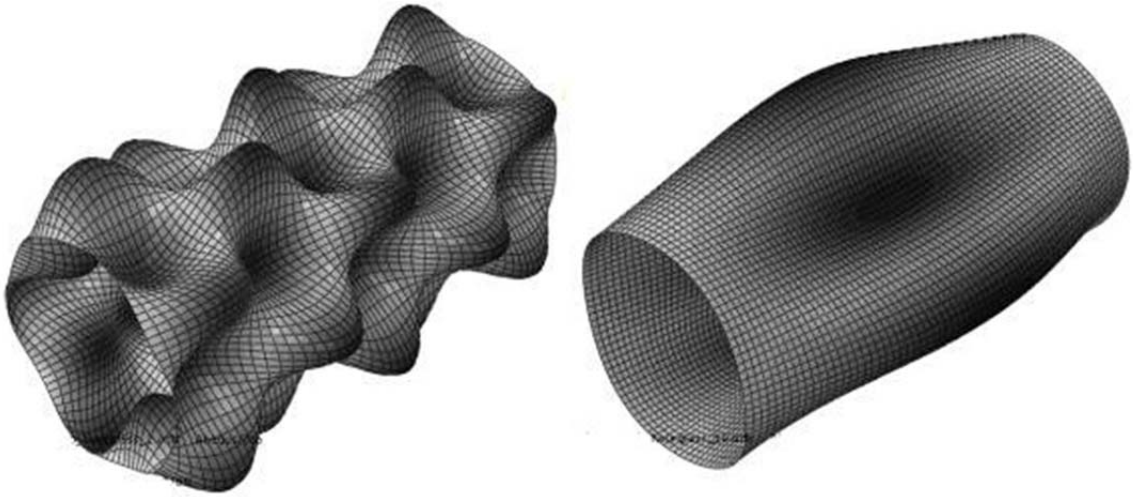

Figure 61 - Comparison of Double Carbon 0.02in and 0.10in Hourglass

Bulge

The bulge shape was the inverse of the hourglass shape – the middle increased diameter and the edges decreased diameter. Modeled with the diameter varying in proportion to height, a full sine wave, with amplitude *scale*, was used with the peak in the center and the troughs at the ends. The bulge shape originated from the same manufacturing inconsistencies as the hourglass and the differentiation between these shapes was based on where the individual specimens were cut from the master tube. The bulge magnitude was computed as the negative of Equation 15.

To translate from rectangular coordinates to cylindrical coordinates a rotation, θ, is calculated at all points (initially radius is constant for the cylinder). The radius is modified by Equation 15, and nodal locations are converted back to rectangular coordinates. Using a 10x exaggeration over the largest bulge used in modeling, Figure 62 shows the nodal positions of a bulged cylinder.

This test report shall not be reproduced, except in full, without the written approval of
the AEWC Advanced Structures & Composites Center.

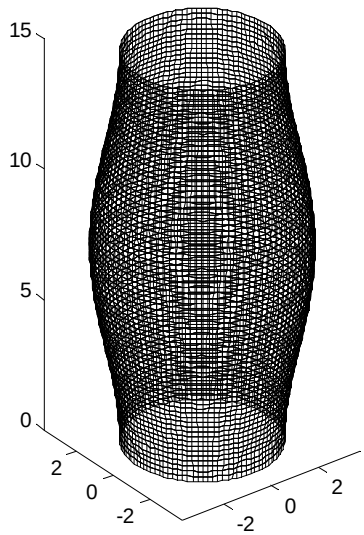

Figure 62 - Wire Mesh of a Bulged Cross Section, 0.984in Radius Increase at Center

Bulging the center of the cylinder did not substantially change the buckling capacity, but it did alter the buckled shape for most models. In Table 30, the largest loss in capacity (4.35%) was the 0.50in bulge in a double carbon model – much smaller than the 22% loss in capacity for the equivalent hourglass shape. In many circumstances, the bulge increased capacity and having a small bulge in the single carbon and bleeder carbon models increased the buckling capacity by as much as 5.1%. Accompanying the change in capacity was a change in buckled shape. No models with a bulge buckled at the mid height of the cylinder – the dominant buckling mode transferred the maximum deformation from the middle to the edge. Even a small bulge (0.02in – too small to be detected by sight) resulting in edge buckling as shown in Figure 63, indicating that buckling mode is very sensitive to a bulge. This is consistent with the large number of bleeder carbon and single carbon specimens that buckled near the edge in bearing-buckling failure. As with no bulge, for double carbon specimens any bulge maintains bearing-buckling failure; experimentally, 7 of 8 specimens failed in bearing-buckling.

This test report shall not be reproduced, except in full, without the written approval of
the AEWC Advanced Structures & Composites Center.

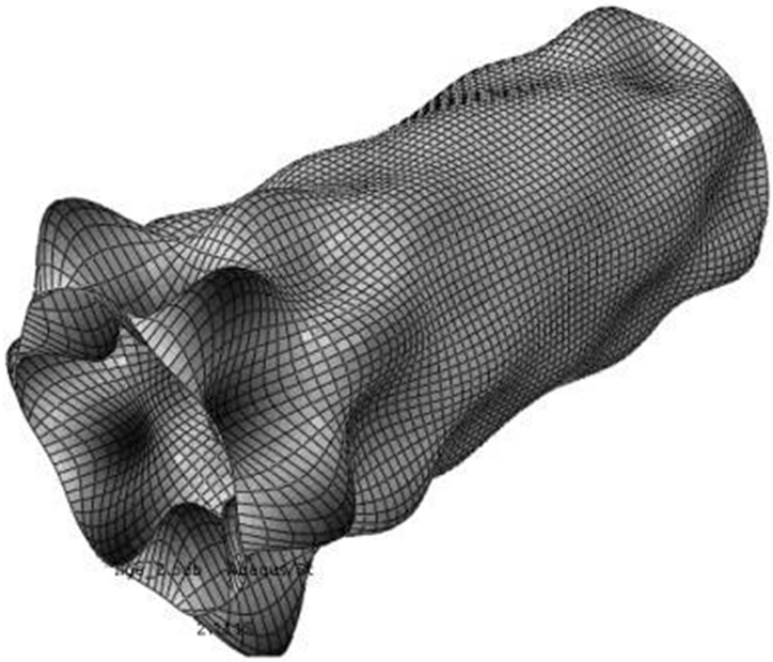

Figure 63 - Buckled Shape, Bleeder Carbon, 0.02in Bulge Perturbation

Elliptical Shape of the Cross-Section

An elliptical cross-sectional shape was not measured in the 6.50in diameter experimental specimens, but it could be caused by improper manufacturing and is a possible side effect of bending stresses (see Bend Testing of Hollow FRP Tubes for a discussion on ovalization). The perimeter of the ellipse is the same as the regular circular cross section, only the minor radius is smaller by a length of *scale* and the major radius is longer by a compensating amount. Where r_A and r_B are the radii, perimeter was calculated using the second Ramanujan approximation, Equation 16 (Sykora 2010), which matches the Taylor series expansion up to the 9th order.

$$perimeter = \pi\left(r_A + r_B\right)\left[1 + \frac{3\left(\frac{\left(r_A - r_B\right)^2}{\left(r_A + r_B\right)^2}\right)}{10 + \sqrt{4 - 3\left(\frac{\left(r_A - r_B\right)^2}{\left(r_A + r_B\right)^2}\right)}}\right] \qquad \text{Equation 16}$$

This test report shall not be reproduced, except in full, without the written approval of
the AEWC Advanced Structures & Composites Center.

This equation was used in conjunction with an iterative process to input a given perimeter and minor radius A to find the major radius B (the circular radius is initially assumed). Figure 64 shows a wire mesh of the modified shape using a 0.984in reduction in the minor radius (from a circular 3.25in radius) and the resulting major radius to keep a constant perimeter. The elliptic shape is exaggerated by a factor of 2.

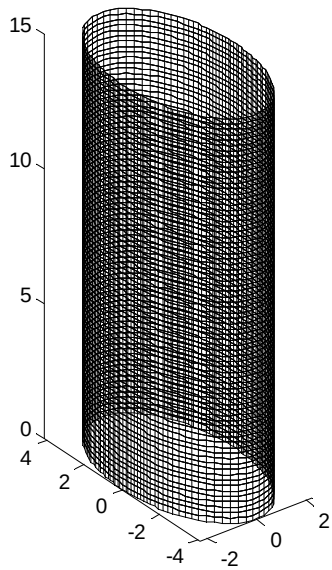

Figure 64 - Wire Mesh of Ellipse Cross Section, Minor Radius Reduced 0.984in

Elliptic perturbation had a smaller effect on capacity than some other perturbations, including the hourglass shape (Table 30). The worst-case ellipse (single carbon 15.4% reduction in minor axis) produced a reduction of 17%, a significant amount, but smaller than hourglass or curvature effects. The least severe ellipse (3.08% reduction in minor axis) was closer to the actual elliptical shape recorded during bending tests (see Bend Testing of Hollow FRP Tubes). They produced a modest 1.0% decrease in the double carbon capacity. Bending specimens should see a reduction in capacity from ellipse shaping, bending stress warps the cross section into an ellipse. Ellipse shaping was negligible on the tested compression specimens.

Elliptical cross sections have a different buckled shape from the circular control that depends on radius change. In Figure 65 a small reduction in radius (0.10in) retains the buckled shape of a circular section while the severe ellipse has little deformation at the middle and has heavy wrinkling on the minor axes near the edges. Double carbon, in

This test report shall not be reproduced, except in full, without the written approval of
the AEWC Advanced Structures & Composites Center.

Figure 66, had a less pronounced shape change between different ellipses. A small radius reduction kept heavy deformations along both axes and a large radius reduction concentrated buckling deformation on the minor axes, but both had buckled shapes dominated by edge effects.

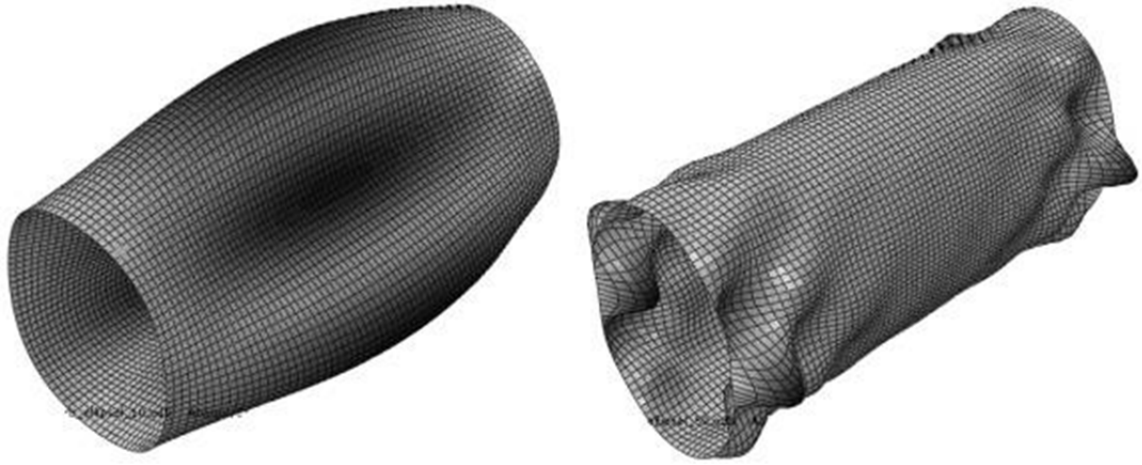

Figure 65 - Single Carbon: 0.10in, 0.50in Minor Radius Loss

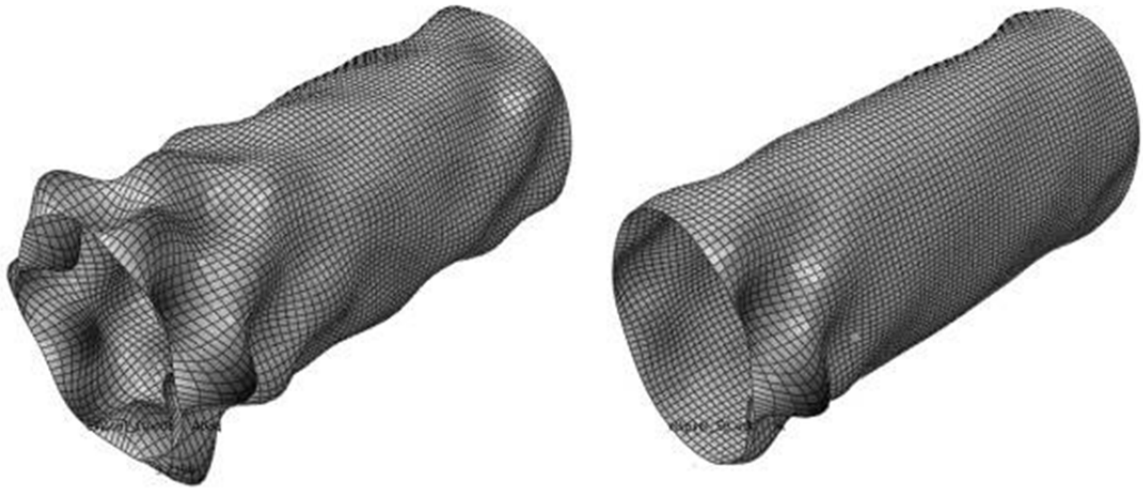

Figure 66 - Double Carbon: 0.10in, 0.50in Minor Radius Loss

Curvature of Section

Experimental specimens were constructed as nominally straight tubes, and an effort was made to manufacture every tube to be as straight as possible. However, some tubes still had locally curved sections. A similar analogy can be made for arches where certain sections are not as tight against the formwork as anticipated and an irregular curvature

This test report shall not be reproduced, except in full, without the written approval of
the AEWC Advanced Structures & Composites Center.

occurs. All of the long, 6.50in diameter tubes except tube SC 165, 1 had a curvature measurement taken, which was reported as a deviation from a central line every 12.0in in length along the tube. This information is in Bend Testing of Hollow FRP Tubes. The tube was placed on supports as in the next section with a tensioned line over the tube positioned at the center points of the tube over the supports. A square with a level was used to find the flat portion at the top of the cross section of the tube and measure the distance from this flat spot to the line. The variation over 12.0in was as high as 1.26in, but a more typical value was .118in to 0.39in. The 1.26in curved section at the center of tube 3 was not used for compression testing. In the model, three perturbations were made including 0.10in (the typical variation), 0.06in (higher than typical but near or below the maximum of every long tube), and 0.50in (higher than the maximum for most tubes but much lower than the absolute maximum of 1.26in). Three general models were created to reflect the inconsistent curvature of the longitudinal specimens: single curvature (cross section is perturbed into a half sine wave shape with ends parallel), double curvature (cross section is perturbed into a half sine wave top and bottom – ends are parallel but do not occupy same x and y coordinates), and a circular arc. In all cases, a portion of the tube – either the top end or the center – is deflected by a magnitude of the variable *scale*. All three perturbations are based on maintaining the perfect uniform circular cross section, but the arc formulation rotated the cross section.

Braid angle fluctuation is ignored in this analysis. Curved tubes do not have a constant fiber angle. Bending the specimen puts increased tension on the outer face (smaller braid angle, increased stiffness) and compression on the inner face (larger braid angle, decreased stiffness). The model implemented assumes a constant braid angle and constant material properties. However, it must be noted that the carbon fiber is at a braid angle where a small fluctuation of even one or two degrees from the nominal value is expected to change the longitudinal stiffness as much as 10% based on a micromechanics analysis of the composite cross-section. Any specimen with variable stiffness would behave differently in the buckling analysis than the uniform stiffness model used.

Single Curvature

For single curvature, x coordinates of all nodes were perturbed by Equation 17, where Z is the height of the cylinder at a node and *scale* is the magnitude of perturbation.

$$Y_{change} = scale * \sin\left(\frac{Z\pi}{Z_{\max}}\right) \qquad \text{Equation 17}$$

When Z is zero or Z_{max}, the equation will equal zero (the top and bottom remain in their initial position). Between the top and bottom the cross section is displaced out of plane

This test report shall not be reproduced, except in full, without the written approval of
the AEWC Advanced Structures & Composites Center.

by a sine wave with maximum amplitude *scale*. A half sine wave was selected because it is a smooth continuous function and the buckled shape predicted by Abaqus for a perfect cylinder has a half sine wave shape for the bleeder carbon and single carbon models (with a triple sine wave around the perimeter). Figure 67 shows a wire mesh rendering of the single curvature perturbation at a mid height displacement of 0.984in.

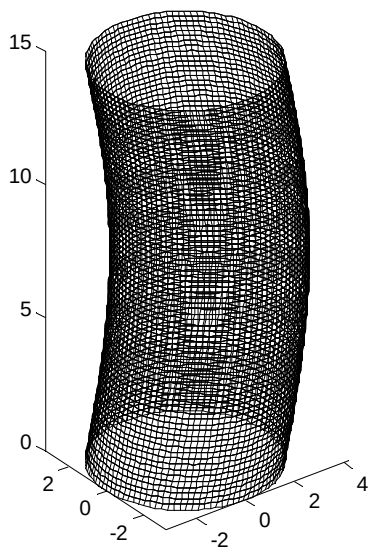

Figure 67 - Wire Mesh of a Single Curvature with 0.984in Perturbation

The single carbon and bleeder carbon models all had the same buckled shape regardless of magnitude. The double carbon models all had a similar shape but the least perturbed model appeared noticeably different from the other two material types. Figure 68 shows the buckled shape of the single curvature perturbation for the (left) bleeder carbon material with a 0.5in center perturbation and the (right) double carbon material with a 0.10in perturbation. Single curvature dominated failures would have appeared as a kink forming at the mid height of the cylinder on a single side of the cylinder – an observed failure for single carbon and bleeder carbon specimens. The least severe double carbon single curvature model produced a shape with maximum deformation at the middle, but high and irregular deformations near the edges.

This test report shall not be reproduced, except in full, without the written approval of
the AEWC Advanced Structures & Composites Center.

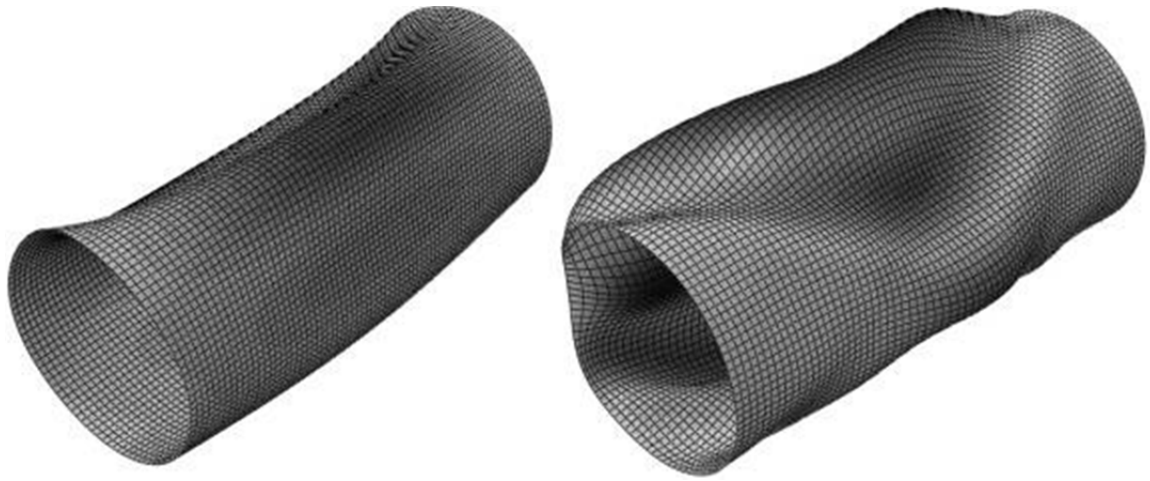

Figure 68 - Single Curvature: Bleeder Carbon 0.5in, Double Carbon 0.10in

Single curvature perturbation produced large reductions in capacity compared to most of the deformed shapes (Table 30). The single curvature model put the center of load away from the centroid of the cylinder, an eccentric load, which produced a bending force in the shell wall and increased the compressive stress on the inside curved face of the cylinder. Reduction of 54% (double carbon) to 61% (single carbon) resulted from a maximum center perturbation of 7.7%. In all three material cases the single curvature perturbation produced buckling loads near or below the average experimental buckling loads, suggesting that this one defect alone – without considering multiple defects, local material stiffness fluctuation, or local wall thickness variation – could have produced the reduction seen from the model to the actual load.

Double Curvature

During manufacture, tubes were hand straightened, but some bends could not be entirely removed. Often, when attempting to straighten a bent section, the result was two bends in close proximity. The magnitude of these bends was large compared to local diameter variations such as the bulge and hourglass, but difficult to correct during manufacture. Models were run where the total displacement over a 6.50in height was 1.7% to 7.7% of the diameter. The double curvature shape has top and bottom cross sections that are both normal to the height of the cylinder but they are not centered at the same location: the top is displaced by the magnitude of the variable *scale* from the bottom face. A conditional set of equations was written in Equation 18.

This test report shall not be reproduced, except in full, without the written approval of
the AEWC Advanced Structures & Composites Center.

If $Z > \frac{Z_{\max}}{2}$ then $Y_{change} = -scale * \sin\left(\frac{Z\pi}{Z_{\max}}\right) + 2$ Equation 18

Else $Y_{change} = scale * \sin\left(\frac{Z\pi}{Z_{\max}}\right)$

The double curvature shape appears incomplete; the cylinder terminates at the points of most rapid bend. The double curvature model is in total a half sine wave imposed on the shape with a quarter sine wave in each direction starting from the center height of the cylinder. This is a single approximation of the many possible specimen imperfections.

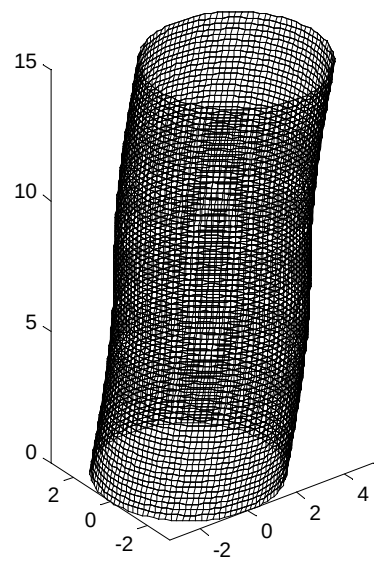

Figure 69 - Wire Mesh of a Double Curvature Section, Top Perturbed 0.984in

Double curvature buckling load reductions were less severe than single curvature models. Instead of reductions near 60% for the 7.7% diameter perturbation, double curvature had reductions from 30% (double carbon) to 42% (single carbon). The buckled shapes for models with double curvature perturbation had a typical failure shape; 8 of 9 had a similar shape to the unperturbed buckling model for the given material. As the double carbon became more perturbed it buckled closer to mid height, as seen in Figure 70. Results were consistent with the observed failures of the experimental specimens where

This test report shall not be reproduced, except in full, without the written approval of
the AEWC Advanced Structures & Composites Center.

the vast majority of double carbon specimens failed near the edge while many of the single carbon or carbon bleeder specimens would fail in the measured gauge length.

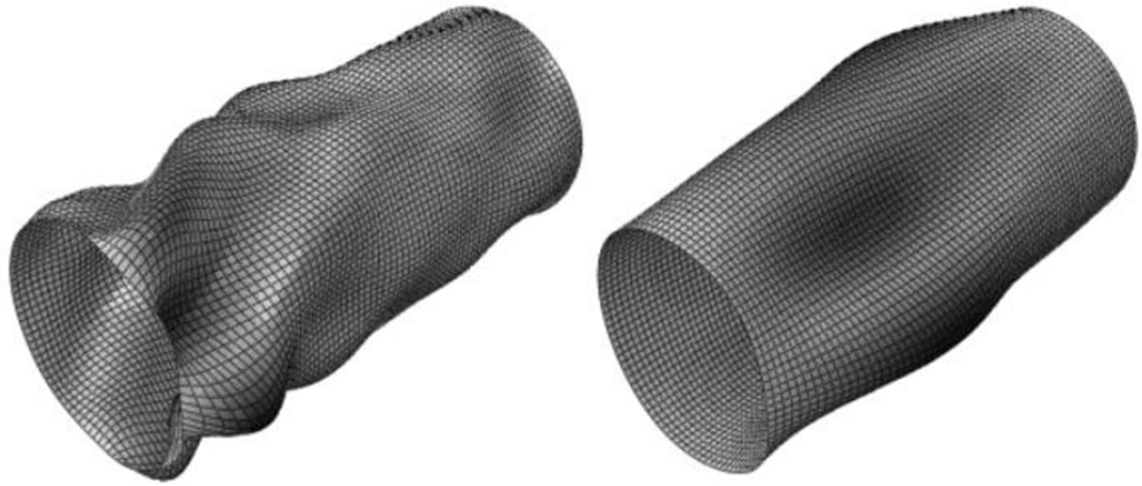

Figure 70 - Double Carbon, Double Curvature 0.10in and 0.5in

Circular Arc

Upon inspection it is impossible to tell whether the organic curvature in a cylinder is closer to a sine wave or a circular arc. The arc perturbation is an important shape that, like the ellipse perturbation, is real and will be in every arch. Unlike the ellipse, the arc shape is used in buried arch bridges. The circular arc was a difficult shape to mathematically construct and an intermediate radius of curvature was calculated, Equation 19

$$radius = \frac{\sqrt{\frac{Z_{\max}^{\ 2}}{2} + scale^2}}{2\cos\left(\frac{\pi}{2} - \arcsin\frac{2Scale}{Z_{\max}}\right)} \qquad \text{Equation 19}$$

This test report shall not be reproduced, except in full, without the written approval of
the AEWC Advanced Structures & Composites Center.

Radius of curvature was used in the expression for calculating the new *Y*, Equation 20 and *Z*, Equation 21, coordinates based on rotating the circular cross section. *X* coordinates remain constant during this analysis.

$$Y_{new} = \cos\left(\frac{\arctan\left(Z - \frac{Z_{\max}}{2}\right)}{radius}\right)(radius - Y) - radius \qquad \text{Equation 20}$$

$$Z_{new} = \sin\left(\frac{\arctan\left(Z - \frac{Z_{\max}}{2}\right)}{radius}\right)(radius - Y) + \frac{Z_{\max}}{2} \qquad \text{Equation 21}$$

Figure 71 shows a deformed cross sectional shape with a 1.0in perturbation at mid height. A difference between this model and the similar single curvature model was that the load rotates with this model to follow the rotation of the shell instead of performing a p-delta analysis; this rotation is more indicative of the stresses propagating through the shell of an arch as opposed to a compression test.

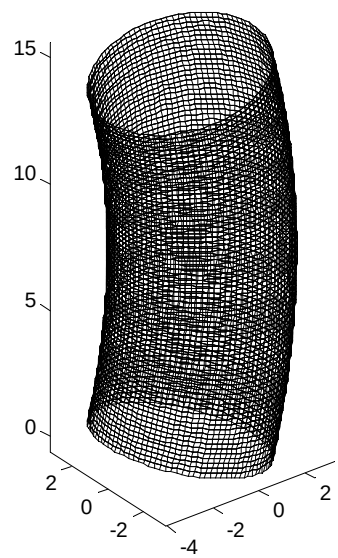

Figure 71 - Wire mesh of an Arc Deflection, Middle Perturbed 1.00in

This test report shall not be reproduced, except in full, without the written approval of the AEWC Advanced Structures & Composites Center.

In Table 30, buckling loads for perturbed models, the double carbon 0.10in arc shows an increase in capacity of 14% over the perfect cylinder. This implied that moderate arc curvature of the cylinder helps the buckling capacity. The steep curvature models, 0.5in centerline perturbation, – beyond what has been intentionally manufactured, but in the range of possible defects – has a severe reduction in capacity similar to the single curvature model (56% reduction in the single carbon capacity). The single curvature and the arc curvature models both impose a central bend in the cylinder, and at the extreme range of what was measured this defect alone was capable of reducing the capacity by over 50%, giving a buckling load near the experimental average. The deformed shape (Figure 72) from this analysis was in all cases very similar to the deformed shape from the single curvature model.

Figure 72 - Double Carbon with 0.5in Arc Perturbation

Eigenvalue Buckling Analysis of Tubes with Holes

When arches are concrete filled with concrete from the apex, a hole drilled into the apex compromises the cross sectional rigidity and the capacity of the compressive face of the arch. A principal reason for building a finite element model was to see the effect of the filling hole on buckling capacity. Experimental reductions in axial compressive capacity can be compared to model reductions as a way of verifying the effect of a hole on structural integrity. Three lay-ups are considered: bleeder-carbon with a small hole, double-carbon with a small hole and double-carbon with a large hole. Hole sizes are the same as those in the test specimens.

Models Without Damage Around Hole

The typical cylinder from previous sections was defined in the parts module. A new part was defined – a solid circular cylinder of diameter 1.75in for the small hole and 3.0in for the large hole – reflecting the holes cut into the experimental specimens. The Abaqus

This test report shall not be reproduced, except in full, without the written approval of
the AEWC Advanced Structures & Composites Center.

'cut instance' tool was used in the assembly module to cut the initial shell cylinder with the new solid cylinder, as a cylindrical hole saw removed a section from the experimental specimens. All other properties – element type, mesh size, and material properties – remained the same from Mesh Refinement, an ideal cylinder.

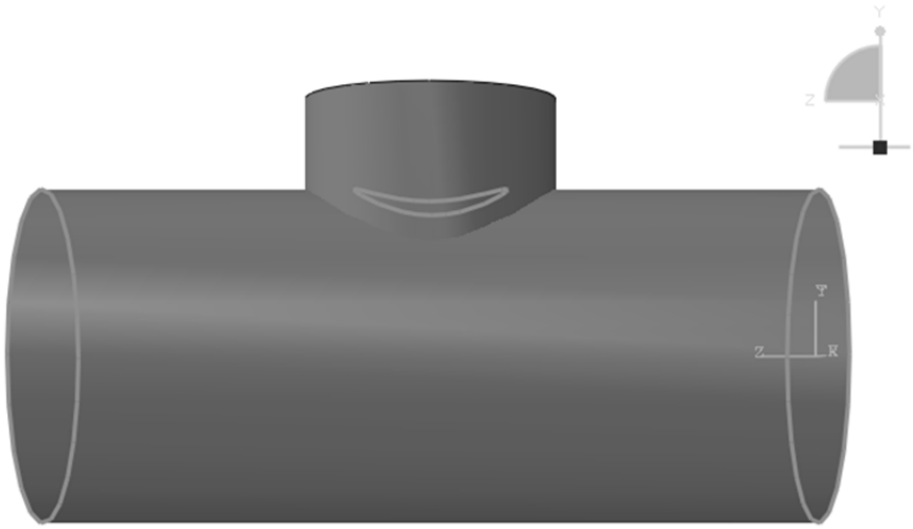

Figure 73 - Cutting a Hole in a Cylinder ABAQUS Model

Adding a hole produced a sizeable reduction in capacity (for the bleeder carbon: 27.9kip, a reduction of 41%) results for all three models with holes are in Table 31. The buckling mode changed from the sine wave shapes typical for a perfect cylinder to a concentrated deformation around the hole. The deformed shape was not consistent with the experiment as the model predicted large creases in the cylinder face, Figure 74, and experimental testing, Figure 76, showed creases at the sides of the cylinder with the top and the bottom face of the cylinder rotating towards the center.

This test report shall not be reproduced, except in full, without the written approval of
the AEWC Advanced Structures & Composites Center.